On the reconstruction of the near-surface seismic motion

Bruno Guidio[a], Heedong Goh[b], Loukas F. Kallivokas[c,d], Chanseok Jeong[a,e,*]

[a] *School of Engineering and Technology, Central Michigan University, Mount Pleasant, 48859, MI, USA*
[b] *Chandra Department of Electrical and Computer Engineering, The University of Texas at Austin, Austin, 78712, TX, USA*
[c] *Department of Civil, Architectural and Environmental Engineering, The University of Texas at Austin, Austin, 78712, TX, USA*
[d] *Oden Institute for Computational Engineering and Sciences, The University of Texas at Austin, Austin, 78712, TX, USA*
[e] *Earth and Ecosystem Science Program, Central Michigan University, Mount Pleasant, 48859, MI, USA*

Abstract

Assessing the built environment's seismic risk relies increasingly on numerical simulations of the response of infrastructure components to seismic motion. Since forecasting earthquake-induced motion is difficult, if not impossible, subjecting the infrastructure to seismic motion from past earthquakes remains the most potent way to assess the infrastructure's risk and resilience. However, such simulations require a rupture-to-rafters modeling approach that entails complex inversion procedures and ultra-scale computations.

In this work, we discuss a systematic methodology that attempts to reconstruct the earthquake-induced wavefield *only* within the near-surface deposits, using ground surface recordings of seismic motion. The methodology improves on alternative approaches by bypassing the need for either seismic source inversion or joint seismic-source-and-material-model inversion, relying instead on *a priori* knowledge of the soil properties for only the near-surface deposits, thus realizing significant computational savings.

The methodology takes advantage of a state-of-the-art, near-surface, seismic wave motion simulation framework rooted in the Domain Reduction Method (DRM), which relies on a reduced computational domain containing the near-surface deposits only, including possible topographic features and even accounting for materially-nonlinear response. The reduced domain is surrounded by an artificial boundary – the DRM boundary –, onto which the seismic input is typically prescribed in forward seismic motion simulations. A narrow wave-absorbing buffer exterior to the DRM boundary completes the computational domain. It is the aim of this work to reconstruct the DRM seismic input from ground-surface records using an inversion approach rooted in partial differential equation (PDE)-constrained optimization, without having to appeal to fault rupture inversion or joint inversions. To this end, we use the DRM, enhanced with a Complex-Frequency-Shifted (CFS) Perfectly-Matched-Layer (PML), to address the forward wave simulation, and an adjoint approach to address the inversion of the DRM seismic input.

Our numerical experiments demonstrate the versatility of the methodology in reconstructing the near-surface seismic motion from sparse surface motion records, almost irrespective of the azimuthal coherency of the incoming motion.

Keywords: Inversion of effective seismic forces, Reconstruction of seismic wavefield, Domain reduction method (DRM), Non-convolutional CFS-PML, Full-waveform inversion, Passive seismic inversion, Earthquake engineering.

1. Introduction

We are concerned with the fidelity of near-surface numerical simulations of seismic motion. The interest stems from the, ever-present, need to assess seismic risk to infrastructure systems. Since the current state of knowledge prevents accurate forecasting of an earthquake to any degree of usefulness, the assessment of seismic risk is, perforce, conducted through studies of the effects past seismic events could have on the infrastructure. This rationale has long

*Corresponding author
Email address: jeong1c@cmich.edu (Chanseok Jeong)

been acknowledged in seismic codes, where seismic response analyses are required to be performed for infrastructure systems using, for example, ground acceleration records of past earthquakes.

While the last few decades have been marked by considerable advances in both computational power and in our ability to ever more faithfully simulate earthquake-induced ground motion, the reliance on one-dimensional models for, for example, site analyses [1, 2], and seismic motion deconvolution [3–5], persists. Central to our ability to assess seismic risk within the described rationale, is not only the ability to depart from one-dimensional models and graduate to two- and three-dimensional models, but also the ability to accurately describe both the subsurface properties and the seismic source. How could the latter, in particular, be accomplished? The most reliable information we have from past events are the ground surface motion records: ideally, the recorded surface motion can serve to infer both the subsurface properties and the source characteristics, usually in the context of joint inversion. Joint inversion entails the computationally daunting task of estimating the properties of the subsurface together with the fault rupture characteristics, following the adoption of suitable material models for the subsurface, a model for the fault rupture, and discretization of the computational domain from the depths of the earth where the faults are located, all the way to the ground surface. Even under the assumption of a linear material model, there can easily result tens to hundreds of millions of material property unknowns that need to be inverted for. Consider, for example, the forward simulation of a 1994 Northridge earthquake aftershock in the San Fernando Valley in California that was attempted some 30 years ago [6]: even after relaxing mesh quality considerations, a volume of 54 km long by 33 km wide by 15 km deep (to capture the fault), would result in about 40 million material property unknowns (two wave velocities and one mass density per material point in a mesh of 13 million nodes). The task of inverting for all these parameters remains an open challenge despite many attempts to date, including successful inversions made possible only under constrained conditions [7, 8].

Given the computational complexity of joint inversion, it stands to reason to question the practicality of such inversions. An easy answer is that knowledge of the subsurface properties and of the source characteristics would allow us to perform true rupture-to-rafters seismic event simulations by adding infrastructure components to the ground surface in a fully-coupled soil-structure model that would now allow modeling the infrastructure's response to incoming (past) seismic motion, while including the seismic source in the model. This, too, is a computationally costly procedure, often demanding high-performance computing resources [9]. To reduce the computational demands, it is often the case that three-dimensional seismic motion simulations are performed on a reduced computational domain using the Domain Reduction Method (DRM) [10, 11] that affords the inclusion of topographic features and/or regions exhibiting nonlinear behavior within a limited near-surface computational domain (Fig. 1). Typically, the DRM partitions the computational domain into two domains, one interior to the DRM boundary and one exterior, where the latter is usually terminated with an absorbing boundary condition or a wave-absorbing buffer, tasked with mimicking the propagation of the outgoing waves in the unbounded physical domain that is excluded from the computations.

A key requirement of the DRM, and central to the near-surface seismic motion computations, is the need to prescribe the incoming seismic motion on the DRM boundary: to date, the seismic input on the DRM has been, by and large, prescribed in the form of idealized motion (e.g., a plane wave), typically unrelated to the actual input/motion induced by a real earthquake. It is the aim of this article to bridge this gap, by providing a systematic approach that allows the determination of the seismic input on the DRM boundary based on ground surface records. We, thus, argue that, for the purpose of near-surface seismic motion simulations, it is not necessary to consider a rupture-to-rafters approach, but instead to use the surface records to invert for the seismic input on the DRM boundary, and then to prescribe on the DRM boundary the inverted-for seismic input in order to fully reconstruct the total seismic wavefield within the near-surface deposits. In this manner, one always stays within the near-surface (computational) confines, without ever venturing into the (computationally) treacherous path of joint inversion that engages huge computational domains and entails significant cost.

To this end, we build upon recent work on a related problem that pertained to the scalar SH case [12], and extend it here to the all-important elastic/seismic wave case. Specifically, we start by first deploying a state-of-the-art framework for the forward problem, i.e, for the numerical simulation of the propagation of seismic (elastic) waves in the near-surface and in the time-domain [13–15]. The forward simulation engine consists of: (*i*) the DRM partitioning scheme [10] that allows the computation of the total and scattered wavefields within the domains interior and exterior to the DRM boundary, respectively; and (*ii*) a Complex-Frequency-Shifted-Perfectly-Matched-Layer (CFS-PML) wave-absorbing buffer [16, 17] that surrounds the domain exterior to the DRM boundary and results in the effective absorption of the outgoing scattered motion.

Our goal, then, is to use the surface motion records to invert for the seismic input, which is expressed in terms of forces applied on the DRM boundary. To this end, we follow classic lines of partial differential equation (PDE)-constrained optimization, whereby we seek to minimize the misfit between the recorded motion at the surface sensors and the motion at the same sensor locations that would result from trial seismic forces prescribed on the DRM boundary, constrained only by the governing PDEs. Among a few alternatives for imposing the latter constraint (e.g., strong or weak form of the continuous PDEs), herein we adopt a discretize-then-optimize (DTO) approach [18, 19] according to which we side-impose to the misfit functional the space-time-discrete form of the governing PDEs (discretized in space and time). We use an adjoint method to recover the sought-after seismic forces on the DRM boundary by satisfying the Karush-Kuhn-Tucker conditions. As discussed in section 4.3, the inverted-for DRM forces suffer from solution multiplicity, but the resulting total wavefield in the domain interior DRM appears unique, and exceedingly well-reconstructed close to the free surface: this is likely due to the implications of the Cauchy-Kovalevskaya theorem [20], as also discussed in section 4.3.

We note that, in addition to the aforementioned computationally-expensive joint inversion approaches, there have also been a few other attempts reported in the literature for the characterization of the incoming seismic motion in the near surface deposits using measured ground motion data: though less computationally expensive, they are also less effective in reconstructing the near-surface seismic motion. Among them, Ghahari et al. [21] and Ghahari et al. [22] studied methods to simultaneously identify the transfer function of a soil column and the incident wave, using recorded signals at two or more stations, while also accounting for uncertainty. Li et al. [23] argued that body waves should be inverted for realistic and comprehensive assessment of seismic effects on structures, but their wavefield-inversion methodology inverted only the incident angles of idealized incoming plane waves. We note that, in the aforementioned studies, the characterized seismic inputs have been limited to propagating plane waves impinging on the free surface at a single angle of incidence. In contrast, herein, we are interested in reconstructing the seismic wavefield while allowing for azimuthally incoherent incident waves.

Herein, the theory and numerical experiments are described for two spatial dimensions: the extension to three dimensions requires that a 3D forward DRM wave simulation engine be used (see, for example, Poursartip et al. [13], endowed with 3D PMLs (Fathi et al. [24])); however, the rest of the technical ingredients remain the same, and, even though the computational cost would increase, we expect the seismic motion reconstruction to be feasible and to exhibit similar performance as the one we report in section 5. Overall, the quality of the near-surface seismic motion reconstruction depends chiefly on the density of the ground surface sensor network.

2. The seismic input and the DRM

To describe the inversion process that leads to the determination of the seismic wavefield within the near-surface deposits using the ground-surface records, it is necessary to introduce the forward modeling framework, which rests on the Domain Reduction Method (DRM) [10]. The DRM is simply the means by which *any* incoming seismic motion can be effectively replaced by a set of forces that act on an artificial boundary –henceforth referred to as the DRM boundary– enveloping the near-surface domain of interest. To this end, consider the computational domain depicted in Fig. 1(a); the originally unbounded domain has been rendered finite through the introduction of a wave-absorbing buffer $\Omega_{\text{CFS-PML}}$, and the resulting finite computational domain has been partitioned into an interior domain Ω_i and an exterior domain Ω_e through the introduction of Γ_{DRM} –the DRM boundary. We assume that $\Omega_i \cup \Omega_e$ are occupied by linear, heterogeneous, elastic solids –a typical assumption for soils not exposed to strong ground motion. We note though that, in general, and owing to the versatility of the DRM, Ω_i could also be occupied by a nonlinear solid; herein, we treat the linear case only.

Following classic DRM lines and a standard Galerkin approach, the motion within Ω_i and Ω_e can be described by

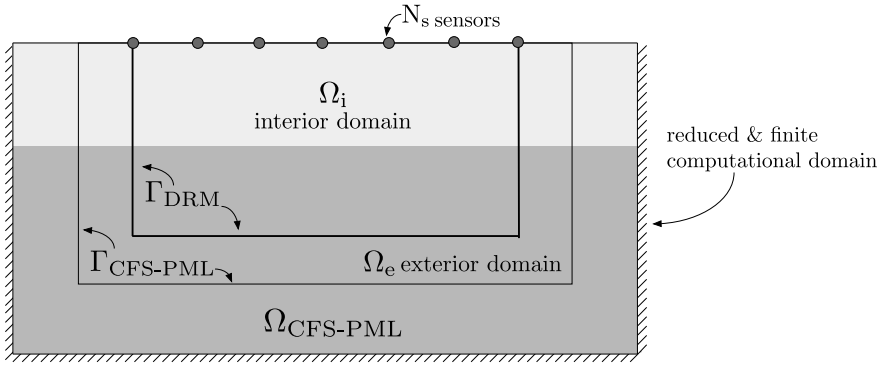

Figure 1: Problem configuration: the originally unbounded domain is replaced by a reduced, finite, computational domain $\Omega_i \cup \Omega_e \cup \Omega_{\text{CFS-PML}}$. Domain Ω_i encompasses the near-surface heterogeneous deposits of interest. The domain partitions are realized through the introduction of the artificial boundaries Γ_{DRM} and $\Gamma_{\text{CFS-PML}}$. N_s sensors are deployed on the ground surface.

the following semi-discrete form[1,2]:

$$\begin{bmatrix} \mathbf{M}_{ii}^{\Omega_i} & \mathbf{M}_{id}^{\Omega_i} & \mathbf{0} \\ \mathbf{M}_{di}^{\Omega_i} & \mathbf{M}_{dd}^{\Omega_i} + \mathbf{M}_{dd}^{\Omega_e} & \mathbf{M}_{de}^{\Omega_e} \\ \mathbf{0} & \mathbf{M}_{ed}^{\Omega_e} & \mathbf{M}_{ee}^{\Omega_e} \end{bmatrix} \begin{bmatrix} \ddot{\mathbf{U}}_i \\ \ddot{\mathbf{U}}_d \\ \ddot{\mathbf{W}}_e \end{bmatrix} + \begin{bmatrix} \mathbf{K}_{ii}^{\Omega_i} & \mathbf{K}_{id}^{\Omega_i} & \mathbf{0} \\ \mathbf{K}_{di}^{\Omega_i} & \mathbf{K}_{dd}^{\Omega_i} + \mathbf{K}_{dd}^{\Omega_e} & \mathbf{K}_{de}^{\Omega_e} \\ \mathbf{0} & \mathbf{K}_{ed}^{\Omega_e} & \mathbf{K}_{ee}^{\Omega_e} \end{bmatrix} \begin{bmatrix} \mathbf{U}_i \\ \mathbf{U}_d \\ \mathbf{W}_e \end{bmatrix} = \begin{bmatrix} \mathbf{0} \\ -\mathbf{M}_{de}^{\Omega_e} \ddot{\mathbf{U}}_e^0 - \mathbf{K}_{de}^{\Omega_e} \mathbf{U}_e^0 \\ +\mathbf{M}_{ed}^{\Omega_e} \ddot{\mathbf{U}}_d^0 + \mathbf{K}_{ed}^{\Omega_e} \mathbf{U}_d^0 \end{bmatrix} \stackrel{\text{def}}{=} \begin{bmatrix} \mathbf{0} \\ \mathbf{P}_{\Gamma_{\text{DRM}}} \\ \mathbf{P}_{\Gamma'_{\text{DRM}}} \end{bmatrix} \stackrel{\text{def}}{=} \mathbf{F}_{\text{DRM}}. \quad (1)$$

In (1), subscripts i, d, and e refer to matrix and vector partitions pertaining to the interior domain Ω_i, the DRM boundary Γ_{DRM}, and the exterior domain Ω_e, respectively. For example, $\mathbf{K}_{ii}^{\Omega_i}$ is the stiffness matrix assembled from elements whose nodes lie entirely in the interior of Ω_i, whereas $\mathbf{K}_{id}^{\Omega_i}$ is the stiffness matrix assembled from finite elements that lie in Ω_i and have at least one node on the DRM boundary Γ_{DRM}. Similarly, $\mathbf{K}_{dd}^{\Omega_i}$ refers to stiffness matrix elements engaging nodes on Γ_{DRM} only, but stemming from finite elements that lie in Ω_i, whereas $\mathbf{K}_{dd}^{\Omega_e}$ refers to similar matrix elements engaging nodes on Γ_{DRM}, yet stemming from finite elements that lie within Ω_e.

Moreover, we use lowercase letters to refer to the various continuous wavefields (e.g., $\mathbf{u}_i$), and uppercase letters (e.g., $\mathbf{U}_i$) to refer to their discrete counterparts. Thus, $\mathbf{U}_i$ and $\mathbf{U}_d$ denote the vectors of nodal values of the total (displacement) wavefields $\mathbf{u}_i$ and $\mathbf{u}_d$ in Ω_i and on Γ_{DRM}, respectively, whereas $\mathbf{W}_e$ denotes the vector of nodal values of the scattered (displacement) wavefield $\mathbf{w}_e$ within the exterior domain Ω_e. In the right-hand-side of (1), according to DRM theory, the fields with zero (0) superscript refer to the displacement field that would have resulted had the interior domain Ω_i, which may include topographic features, heterogeneities, or other nonlinearities, been replaced by a domain where these particular features had been removed/simplified: in the parlance of the DRM, the zero-superscripted fields are referred to as the free-field motion.

Of critical importance to both the forward modeling and the ensuing inversion is understanding the role that the right-hand-side of (1) plays in the modeling: owing to the particular structure of the matrix-vector products involved, the resulting vectors $\mathbf{P}_{\Gamma_{\text{DRM}}}$ and $\mathbf{P}_{\Gamma'_{\text{DRM}}}$ refer to (effective) forces that are applied only on Γ_{DRM} and on Γ'_{DRM}, respectively. Γ_{DRM} is, as previously defined, the interface separating the interior domain Ω_i from the exterior domain Ω_e, whereas Γ'_{DRM} encompasses all the nodes in the first-most layer of elements in Ω_e, adjacent to Γ_{DRM}, but exclusive of the nodes on Γ_{DRM} (Fig. 2). Typically, the DRM layer is only one-element wide, sandwiched between Γ_{DRM} and Γ_e (Fig. 1): if, for example, the DRM layer consists of bilinear quadrilaterals (Fig. 2a), then $\Gamma'_{\text{DRM}} \equiv \Gamma_e$; if, in contrast, the DRM layer consists of biquadratic elements, then $\Gamma'_{\text{DRM}} \equiv \Gamma_e \cup \Gamma_m$ (Fig. 2b).

[1] For brevity, the semi-discrete form (1) is written assuming lossless soil deposits; damping matrices exhibiting a similar structure to the mass and stiffness matrices can be added to account for lossy soils under viscous damping assumptions.

[2] To avoid notational congestion and maintain the focus on the DRM, the effect of the CFS-PML buffer has not been included in (1); it is restored later in equation (2).

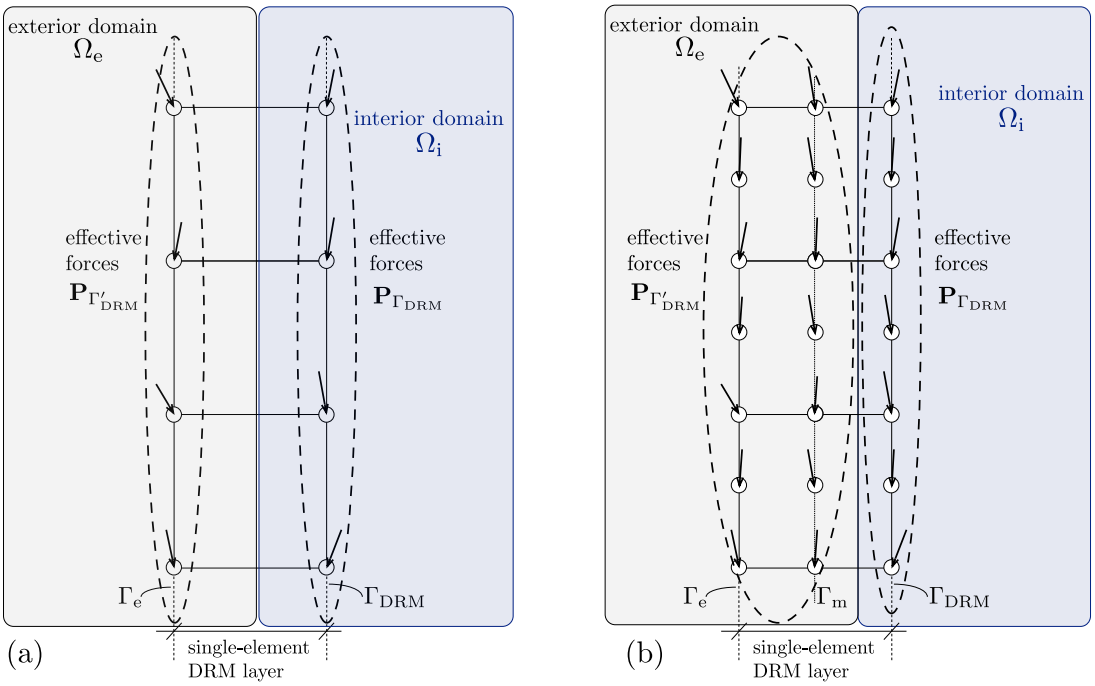

Figure 2: Typical topology of a DRM layer and associated effective forces; (a) the DRM layer consists of bilinear quadrilaterals; (b) the DRM layer consists of biquadratic quadrilaterals.

The effective forces $\mathbf{P}_{\Gamma_{DRM}}$ and $\mathbf{P}_{\Gamma'_{DRM}}$ capture the incoming seismic motion to its fullest extent, and account for all of its characteristics, including directionality, frequency content, and propagation path. To use the effective forces in a forward modeling setting, it is necessary to obtain first the free-field motion $\mathbf{u}^0$: this requires *a priori* knowledge of the seismic source characteristics and of the earth's (linear) properties from the source (rupture fault) to the ground surface. But, in an inverse setting, it is precisely $\mathbf{P}_{\Gamma_{DRM}}$ and $\mathbf{P}_{\Gamma'_{DRM}}$ that we are interested in inverting, informed only by the ground-surface records, i.e., by $\mathbf{u}_i$ on the ground surface, *without any need for a priori information on the source or the earth's properties at depth*[3]. Thus, for inversion purposes, the free field motion $\mathbf{u}^0$ needs *never* be computed.

It is important to note that the wavefields in (1) exhibit, by design, a discontinuity on the DRM boundary: $\mathbf{u}_i$ and $\mathbf{u}_d$ are the *total* wavefields *interior* to Γ_{DRM} and *on* Γ_{DRM}, respectively, whereas $\mathbf{w}_e$ is the *scattered* wavefield, *exterior* to Γ_{DRM}. In fact, it is the effective forces $\mathbf{P}_{\Gamma_{DRM}}$ and $\mathbf{P}_{\Gamma'_{DRM}}$ that are responsible for imparting the discontinuity between the two wavefields ($\mathbf{u}_d$ and $\mathbf{w}_e$) across Γ_{DRM}, and are themselves discontinuous (there is a jump between $\mathbf{P}_{\Gamma_{DRM}}$ and $\mathbf{P}_{\Gamma'_{DRM}}$): this observation is of importance in assessing the quality of the inversion, as will be discussed.

3. The forward problem

Now that the DRM's technical details have been described, we turn to the complete description of the forward simulator, which encompasses not only the DRM, but also addresses the truncation of the unbounded domain through the introduction of a recently developed Complex-Frequency-Shifted Perfectly-Matched-Layer (CFS-PML) [16, 17]. The particular form of the CFS-PML we adopted allows us to retain the second-order character of the semi-discrete equations of motion, at the moderate expense of auxiliary CFS-PML variables introduced within the absorptive PML

[3]The properties of the near-surface deposits in Ω_i must be *a priori* known.

buffer. Then, the resulting semi-discrete form for the forward simulation engine becomes:

$$\begin{bmatrix} \mathbf{M}_{ii}^{\Omega_i} & \mathbf{M}_{id}^{\Omega_i} & \mathbf{0} \\ \mathbf{M}_{di}^{\Omega_i} & \mathbf{M}_{dd}^{\Omega_i} + \mathbf{M}_{dd}^{\Omega_e} & \mathbf{M}_{de}^{\Omega_e} \\ \mathbf{0} & \mathbf{M}_{ed}^{\Omega_e} & \mathbf{M}_{ee}^{\Omega_e} + \mathbf{M}_{\mathrm{PML}} \end{bmatrix} \begin{bmatrix} \ddot{\mathbf{U}}_i \\ \ddot{\mathbf{U}}_d \\ \ddot{\mathbf{V}} \end{bmatrix} + \begin{bmatrix} \mathbf{C}_{ii}^{\Omega_i} & \mathbf{C}_{id}^{\Omega_i} & \mathbf{0} \\ \mathbf{C}_{di}^{\Omega_i} & \mathbf{C}_{dd}^{\Omega_i} + \mathbf{C}_{dd}^{\Omega_e} & \mathbf{C}_{de}^{\Omega_e} \\ \mathbf{0} & \mathbf{C}_{ed}^{\Omega_e} & \mathbf{C}_{ee}^{\Omega_e} + \mathbf{C}_{\mathrm{PML}} \end{bmatrix} \begin{bmatrix} \dot{\mathbf{U}}_i \\ \dot{\mathbf{U}}_d \\ \dot{\mathbf{V}} \end{bmatrix} + \begin{bmatrix} \mathbf{K}_{ii}^{\Omega_i} & \mathbf{K}_{id}^{\Omega_i} & \mathbf{0} \\ \mathbf{K}_{di}^{\Omega_i} & \mathbf{K}_{dd}^{\Omega_i} + \mathbf{K}_{dd}^{\Omega_e} & \mathbf{K}_{de}^{\Omega_e} \\ \mathbf{0} & \mathbf{K}_{ed}^{\Omega_e} & \mathbf{K}_{ee}^{\Omega_e} + \mathbf{K}_{\mathrm{PML}} \end{bmatrix} \begin{bmatrix} \mathbf{U}_i \\ \mathbf{U}_d \\ \mathbf{V} \end{bmatrix} = \begin{bmatrix} \mathbf{0} \\ \mathbf{P}_{\Gamma_{\mathrm{DRM}}} \\ \mathbf{P}_{\Gamma'_{\mathrm{DRM}}} \end{bmatrix} = \mathbf{F}_{\mathrm{DRM}}, \tag{2}$$

where $\mathbf{M}_{\mathrm{PML}}$, $\mathbf{C}_{\mathrm{PML}}$, and $\mathbf{K}_{\mathrm{PML}}$, are mass, damping, and stiffness matrices associated with the CFS-PML (detailed expressions can be found in Appendix A), and the vector $\mathbf{V}(t)$ is augmented to now consist of the vector of nodal scattered field displacements $\mathbf{W}_e(t)$ within $\Omega_e \cup \Omega_{\mathrm{CFS-PML}}$, and of the vector of auxiliary PML variables $\boldsymbol{\Theta}(t)$, $\boldsymbol{\Phi}(t)$, and $\mathbf{H}(t)$ (Appendix A). We note that the various damping submatrices in (2) account for lossy soils, following the adoption of suitable soil models that incorporate intrinsic attenuation; various candidate choices for soils that would yield velocity-proportional damping terms (e.g., Generalized Maxwell Body) can be found in [25]. Here, owing to the lossless soils considered in this study, the various damping submatrices in (2) vanish identically, except for $\mathbf{C}_{\mathrm{PML}}$, which is always nonzero due to the presence of the PML buffer. In compact form, equation (2) can be rewritten as the standard second-order set of ODEs:

$$\mathbf{M}\,\ddot{\mathbf{U}}(t) + \mathbf{C}\,\dot{\mathbf{U}}(t) + \mathbf{K}\,\mathbf{U}(t) = \mathbf{F}_{\mathrm{DRM}}(t), \tag{3}$$

where, now, $\mathbf{U}(t)$ encompasses all nodal unknowns, i.e., the total displacements $\mathbf{U}_i(t)$ and $\mathbf{U}_d(t)$, the scattered displacements $\mathbf{W}_e(t)$, and the auxiliary nodal vectors $\boldsymbol{\Theta}(t)$, $\boldsymbol{\Phi}(t)$, and $\mathbf{H}(t)$:

$$\mathbf{U}(t) = \left[\mathbf{U}_i^T(t)\;\; \mathbf{U}_d^T(t)\;\; \mathbf{V}^T(t)\right]^T = \left[\mathbf{U}_i^T(t)\;\; \mathbf{U}_d^T(t)\;\; \mathbf{W}_e^T(t)\;\; \boldsymbol{\Theta}^T(t)\;\; \boldsymbol{\Phi}^T(t)\;\; \mathbf{H}^T(t)\right]^T\;, \tag{4}$$

and

$$\mathbf{F}_{\mathrm{DRM}}(t) = [\mathbf{0}^T \quad \mathbf{P}_{\Gamma_{\mathrm{DRM}}}^T(t) \quad \mathbf{P}_{\Gamma'_{\mathrm{DRM}}}^T(t)]^T \quad . \tag{5}$$

We note that in (5), the force vector $\mathbf{F}_{\mathrm{DRM}}(t)$ has non-zero entries only along Γ_{DRM} and Γ'_{DRM}. By adopting an implicit Newmark time-integration scheme, and by collecting the acceleration-like quantities $\ddot{\mathbf{U}}(t)$, the velocity-like $\dot{\mathbf{U}}(t)$, and the displacement-like $\mathbf{U}(t)$ at all time steps in a single vector $\hat{\mathbf{d}}$, it can be shown that (3) reduces to (see Appendix Appendix B):

$$\mathbf{Q}\,\hat{\mathbf{d}} = \hat{\mathbf{F}}_{\mathrm{DRM}}, \tag{6}$$

where a hat ($\hat{}$) denotes space-time discretization of the subtended quantity. The compact form (6) is *the discrete form of the space-time-discretized forward problem*.

4. Inverting for the seismic input

The inversion for the seismic input is driven by the ground-surface records of motion, collected, typically, in the form of displacement or velocity time histories for each motion component[4]. Given N_{s} sensors situated on the ground surface (Fig. 1), the recorded displacement time histories form the measurement vector $\hat{\mathbf{d}}^{\mathrm{m}}$, with non-zero entries only along the surface.

We define the following discrete objective functional $\hat{\mathcal{A}}$ to capture the misfit between measurements $\hat{\mathbf{d}}^{\mathrm{m}}$ and computed responses $\hat{\mathbf{d}}^{\mathrm{inv}}$; the latter are based on trial distributions of the seismic input $\hat{\mathbf{F}}_{\mathrm{DRM}}^{\mathrm{inv}}$ on the DRM boundary:

$$\hat{\mathcal{A}} = \frac{1}{2}(\hat{\mathbf{d}}^{\mathrm{inv}} - \hat{\mathbf{d}}^{\mathrm{m}})^T\,\overline{\mathbf{B}}\,(\hat{\mathbf{d}}^{\mathrm{inv}} - \hat{\mathbf{d}}^{\mathrm{m}}), \tag{7}$$

[4]If velocities are recorded, then the records are integrated in time to yield displacement time series, which are preferable, since the integration process filters out high-frequency artifacts that are inconsistent with the induced motion.

where $\overline{\mathbf{B}}$ is a block diagonal matrix defined as Δt $\mathbf{B}$, in which $\mathbf{B}$ is a square, diagonal matrix that has zero entries everywhere except for entries of one along its diagonal, which correspond to the sparsely-distributed ground surface sensors nodal locations. Then, we construct a Lagrangian $\hat{\mathcal{L}}$ by side-imposing to the objective functional $\hat{\mathcal{A}}$, using Lagrange multipliers $\hat{\boldsymbol{\lambda}}$, the discrete forward problem (6), written for computed responses $\hat{\mathbf{d}}^{\text{inv}}$ corresponding to trial seismic input $\hat{\mathbf{F}}^{\text{inv}}_{\text{DRM}}$:

$$\hat{\mathcal{L}} = \frac{1}{2}(\hat{\mathbf{d}}^{\text{inv}} - \hat{\mathbf{d}}^{\text{m}})^T \,\overline{\mathbf{B}}\,(\hat{\mathbf{d}}^{\text{inv}} - \hat{\mathbf{d}}^{\text{m}}) - \hat{\lambda}^T(\mathbf{Q}\,\hat{\mathbf{d}}^{\text{inv}} - \hat{\mathbf{F}}^{\text{inv}}_{\text{DRM}}). \tag{8}$$

In accordance to the space-time discretization scheme described in Appendix Appendix B, $\hat{\boldsymbol{\lambda}}$ is the discrete space-time Lagrange multiplier vector defined as $\hat{\boldsymbol{\lambda}} = [\boldsymbol{\lambda}_0^T, \dot{\boldsymbol{\lambda}}_0^T, \ddot{\boldsymbol{\lambda}}_0^T, ..., \boldsymbol{\lambda}_\tau^T, \dot{\boldsymbol{\lambda}}_\tau^T, \ddot{\boldsymbol{\lambda}}_\tau^T]^T$, where a subscript indicates a time step, and τ denotes the final time step. The goal is to find the (space-time discrete) seismic forces $\hat{\mathbf{F}}^{\text{inv}}_{\text{DRM}}$ by minimizing the Lagrangian $\hat{\mathcal{L}}$, thus, simultaneously, enforcing the observations $\hat{\mathbf{d}}^{\text{m}}$ to match the computed responses $\hat{\mathbf{d}}^{\text{inv}}$, while the underlying physics described by equation (6), i.e., $\mathbf{Q}\,\hat{\mathbf{d}}^{\text{inv}} = \hat{\mathbf{F}}^{\text{inv}}_{\text{DRM}}$, are satisfied. To this end, we seek a stationary point for the Lagrangian $\hat{\mathcal{L}}$, as described in the following section.

4.1. First-order optimality conditions

To invert for the unknown seismic input $\hat{\mathbf{F}}^{\text{inv}}_{\text{DRM}}$ on the DRM boundary, we seek to satisfy the first-order optimality conditions. The optimality conditions are obtained as the Fréchet derivatives of the Lagrangian with respect to the Lagrange multipliers $\hat{\lambda}$, the forward response $\hat{\mathbf{d}}^{\text{inv}}$, and the inversion variable $\hat{\mathbf{F}}^{\text{inv}}_{\text{DRM}}$, respectively. Accordingly, the first two derivatives result in:

$$\frac{\partial \hat{\mathcal{L}}}{\partial \hat{\boldsymbol{\lambda}}} = -\mathbf{Q}\,\hat{\mathbf{d}}^{\text{inv}} + \hat{\mathbf{F}}^{\text{inv}}_{\text{DRM}}, \quad \frac{\partial \hat{\mathcal{L}}}{\partial \hat{\mathbf{d}}^{\text{inv}}} = -\mathbf{Q}^T\hat{\lambda} + \mathbf{B}\,(\hat{\mathbf{d}}^{\text{inv}} - \hat{\mathbf{d}}^{\text{m}}). \tag{9}$$

Requiring that the above Fréchet derivatives vanish yields the first two optimality conditions, which, as it can be readily seen, define the following forward and adjoint problems for the forward response $\hat{\mathbf{d}}^{\text{inv}}$ and for the Lagrange multipliers $\hat{\lambda}$, respectively:

$$\underbrace{\mathbf{Q}\,\hat{\mathbf{d}}^{\text{inv}} = \hat{\mathbf{F}}^{\text{inv}}_{\text{DRM}}}_{\text{forward problem}}, \quad \underbrace{\mathbf{Q}^T\hat{\lambda} = \overline{\mathbf{B}}\,(\hat{\mathbf{d}}^{\text{inv}} - \hat{\mathbf{d}}^{\text{m}})}_{\text{adjoint problem}}. \tag{10}$$

We note that the forward problem is driven by trial distributions of the effective forces $\hat{\mathbf{F}}^{\text{inv}}_{\text{DRM}}$, while the adjoint problem is driven by the misfit at the sensor locations. The adjoint problem is also a final-value problem that is resolved by marching backwards in time [26]. Lastly, the third optimality condition leads to the following control equation:

$$\frac{\partial \hat{\mathcal{L}}}{\partial \hat{\mathbf{F}}^{\text{inv}}_{\text{DRM}}} = \hat{\boldsymbol{\lambda}}. \tag{11}$$

That is, the gradient of the Lagrangian with respect to the seismic input (inversion variable) equals the adjoint solution $\hat{\boldsymbol{\lambda}}$. We note that, when the control equation (11) vanishes for an inverted set of seismic input forces $\hat{\mathbf{F}}^{\text{inv}}_{\text{DRM}}$, then $\hat{\boldsymbol{\lambda}} \equiv 0$, and the misfit vanishes identically, while the forward problem is also satisfied. In other words, in such cases, $\hat{\mathbf{F}}^{\text{inv}}_{\text{DRM}}$ is pronounced to be a solution for the seismic input, since all three optimality conditions are satisfied.

4.2. The inversion process

Armed with the technical details described in the preceding section, we discuss next the inversion process in its entirety. The overarching goal is twofold: (a) to recover the seismic forces on the DRM boundary using only the surface records and information about the material properties of the near-surface deposits; and (b) to reconstruct the total wavefield within the near-surface deposits, since such a reconstruction would allow us to assess the response everywhere within the region of interest, setting the stage for a complete post-mortem assessment of the exposed infrastructure. Moreover, the reconstruction of the DRM forces also allows the assessment of future infrastructure additions (or subtractions) to the same seismic scenario, by taking advantage of the DRM theory.

As previously described, the inversion process engages only the reduced, finite, computational domain depicted in Fig. 1, which includes the interior domain Ω_i containing the near-surface deposits of interest, the DRM boundary and its discrete counterpart defined by a single-element layer, sandwiched between the dashed lines Γ_{DRM} and Γ_e (Fig. 2), the (rather limited) exterior domain Ω_e, and the surrounding absorptive buffer $\Omega_{\text{CFS-PML}}$, occupied by the non-convolutional CFS-PML [16, 17]. Without loss of generality, we assume throughout that the incident seismic motion, whether synthetic or real, originates from a location exterior to the reduced computational domain.

The first step involves the synthetic generation of the ground-surface records at the sensor locations: to this end, we turn to an extended computational domain, where the exterior domain Ω_e has been enlarged to now contain a seismic source. The enlarged domain, too, is terminated with a CFS-PML buffer. Herein, we model the seismic source as a body force situated within Ω_e, but several other commonly used seismic source models, including double-couples, plane waves, kinematic fault models, etc., are possible: the presented methodology is *independent* of the seismic source model. Then, using the DRM framework, the free-field response $\mathbf{u}^0$ corresponding to the seismic source is generated first, and, next, with the aid of the expressions involved in the right-hand-side of (1), the effective seismic forces $\mathbf{F}_{\text{DRM}}$ on the DRM boundary are defined. Then, using (2), the total wavefield $\mathbf{u}_i$ is obtained at all nodes within the interior domain of interest Ω_i, and, consequently, on the surface as well: the displacement histories at the N_{s} sensor locations on the ground surface are then used to populate the measurements $\hat{\mathbf{d}}^{\text{m}}$, thus completing the synthetic generation. When actual records are available, the entire first step is omitted, and the synthetic data are replaced by the real sensor data.

The inversion process is initiated with a guess for the seismic forces $\hat{\mathbf{F}}^{\text{inv}}_{\text{DRM}}$, and the forward problem (10)a is solved next, resulting in computed responses $\hat{\mathbf{d}}^{\text{inv}}$. Using the computed responses $\hat{\mathbf{d}}^{\text{inv}}$ and the known measurements $\hat{\mathbf{d}}^{\text{m}}$, the misfit is computed, allowing next for the solution of the adjoint problem (10)b, which yields the Lagrange multipliers $\hat{\lambda}$. Per the control equation (11), the computation of the Lagrange multipliers is used in the gradient definition, which, in turn, drives the updates for the seismic forces $\hat{\mathbf{F}}^{\text{inv}}_{\text{DRM}}$. The updated DRM forces are fed back into the forward problem, and the process is repeated until the third optimality condition is satisfied (adjoint variables vanish). We note that both the horizontal and vertical components of the nodal forces $\hat{\mathbf{F}}^{\text{inv}}_{\text{DRM}}$ at the DRM layer are inverted for: they are the only entries of $\hat{\mathbf{F}}^{\text{inv}}_{\text{DRM}}$ that are non-zero during the inversion iterations. The flowchart of Fig. 3 summarizes the overall inversion process.

4.3. On the multiplicity of the seismic forces

As witnessed in prior work involving the scalar wave case [12], the inverted components of $\hat{\mathbf{F}}^{\text{inv}}_{\text{DRM}}$ differed significantly from the target seismic forces $\hat{\mathbf{F}}_{\text{DRM}}$, despite the fact that there was good agreement between the computed and measured *total* wavefields in the interior domain Ω_i, and, despite the fact that the misfit had vanished. In addition, it was also observed that there was a significant difference in the scattered wavefield in the exterior domain Ω_e: the amplitudes of the scattered motion induced by the inverted seismic forces were significantly larger than those induced by the target (true) seismic input. The same observations were confirmed in the numerical experiments reported herein for the elastic wave case.

To understand the root cause for the discrepancies, it is necessary to describe first the rather uncommon characteristics of the inverse problem at hand. To this end, we note that there are infinite ways by which one can partition the total wavefield $\mathbf{u}_e$ in the exterior domain Ω_e. Specifically, there are infinitely many pairs of incident wavefields $\tilde{\mathbf{u}}^0$ and scattered wavefields $\tilde{\mathbf{w}}_e$, which, when combined, will produce the same total (true) wavefield $\mathbf{u}_e = \tilde{\mathbf{w}}_e + \tilde{\mathbf{u}}^0$ in Ω_e. Using any single one of the fictitious incident fields $\tilde{\mathbf{u}}^0$ in the DRM forces of equation (1), as if it were *a priori* known, would still satisfy the equations of motion, and would still render the true total wavefield $\mathbf{u}_i$ in the interior, but would produce a, possibly, non-physical external wavefield $\tilde{\mathbf{w}}_e$ (e.g., large amplitude scattered motion) . The set of all such possible fictitious incident fields[5] generates a set of DRM force distributions, *all of which constitute admissible solutions for the DRM forces*. In other words, we have an uncommon peculiarity for an inverse problem: whereas in a typical inverse problem, one aims at reducing the solution multiplicity by adopting regularization schemes to filter out unwanted multiples, here, any single one of the DRM force distributions would be admissible (as long as the misfit vanishes). There is, thus, no need for regularization, in the classical sense, and none has been implemented.

[5]The set includes the true pair $\tilde{\mathbf{w}}_e + \mathbf{u}^0$, where $\mathbf{u}^0$ is the free-field motion.

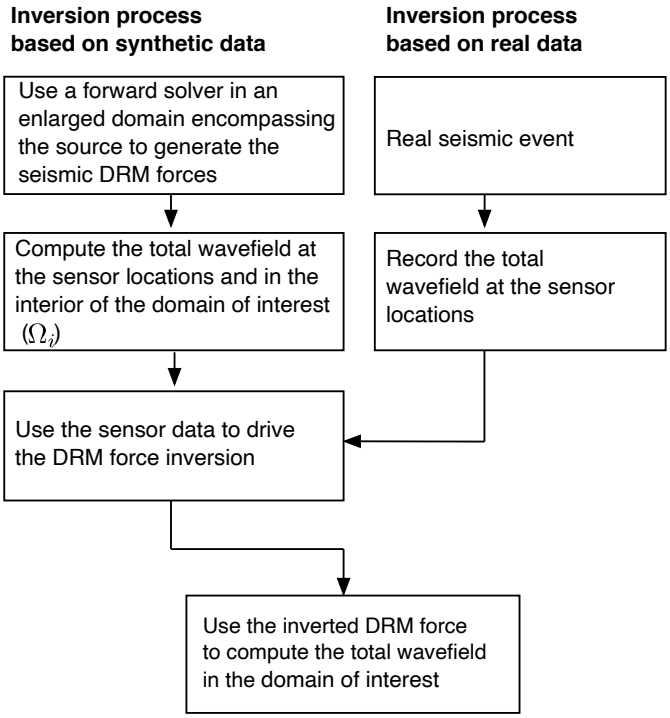

Figure 3: Flowchart of the inversion process for the reconstruction of the seismic DRM forces and the total wavefield in Ω_i. Left column: inversion process based on synthetic data; right column: inversion process based on real data.

We further note that the set of admissible DRM force distributions includes DRM forces that are continuous across the DRM layer, as well as distributions that exhibit a jump, as originally predicated by the DRM theory: any such force distribution would be admissible. Thus, the remaining question is whether the inversion process can converge to any single one of the infinitely many, admissible, DRM force distributions. As it turns out, this is a question of *quality* of the inverted DRM force distributions, and not a question of *uniqueness* of the DRM forces: the inversion process will converge to one of the many candidate DRM force solutions, with the quality of the force reconstruction dependent only on the availability/density of the ground surface data.

The observed difference between the inverted DRM forces and the true DRM forces derived based on the free-field motion is due, primarily, to the fact that the inversion process favors seismic forces at the DRM boundary that are *continuous* across the DRM layer, thereby defeating one of the foundational elements of the DRM theory, which, as discussed in section 2, enforces a partitioning of the wavefields into total for the interior and scattered for the exterior, by imparting a jump in the forces on the DRM layer. But, as argued above, this is not of concern, since the interior total field would still be, by and large, well reconstructed. The latter is likely due to the Cauchy-Kovalevskaya theorem that guarantees the uniqueness of the total wavefield in the neighborhood of the sensor data (but cannot guarantee uniqueness away from the neighborhood), and helps explain the remarkably good reconstruction of the total wavefield near the free surface.

It is for the outlined reasons and owing to the peculiarity of the inverse source problem at hand that, when discussing the numerical results, our focus is on comparisons of the *true* total wavefield in the interior domain of interest against the total wavefield resulting from the inverted DRM forces $\hat{\mathbf{F}}^{\text{inv}}_{\text{DRM}}$, and not on the DRM forces per se.

5. Numerical Experiments

We report numerical experiments aimed at the reconstruction of the seismic forces on the DRM boundary enveloping the near-surface deposits of interest, when given ground surface measurements at a few sensors. Of particular focus is

the method's effectiveness in reconstructing the total wavefield within Ω_i induced by the inverted DRM forces $\hat{\mathbf{F}}^{\text{inv}}_{\text{DRM}}$, when compared with the total wavefield induced by the targeted DRM forces $\hat{\mathbf{F}}_{\text{DRM}}$.

Throughout, we use a reduced computational domain that is 40 m wide by 20 m deep, surrounded along three of its sides by a 10 m-thick PML buffer (Fig. 4(A)). We recall that the DRM is primarily designed to partition the computational domain so that topographical features and/or zones of soil nonlinear behavior be contained within the interior domain Ω_i. In the absence of such features, the DRM placement is driven by the region of interest and considerations of computational efficiency. And, therefore, here, the computational domain is partitioned into the interior domain Ω_i – a 35 m long by 17.5 m deep domain –, which is enveloped by a, relatively thin, exterior domain Ω_e (Fig. 4A).

For the purpose of generating the incident wave motion, we embed the reduced domain within an enlarged domain; the size of the enlarged domain is set to be 80 m by 40 m, and it too is surrounded by a 10 m-thick PML (Fig. 4(B)).

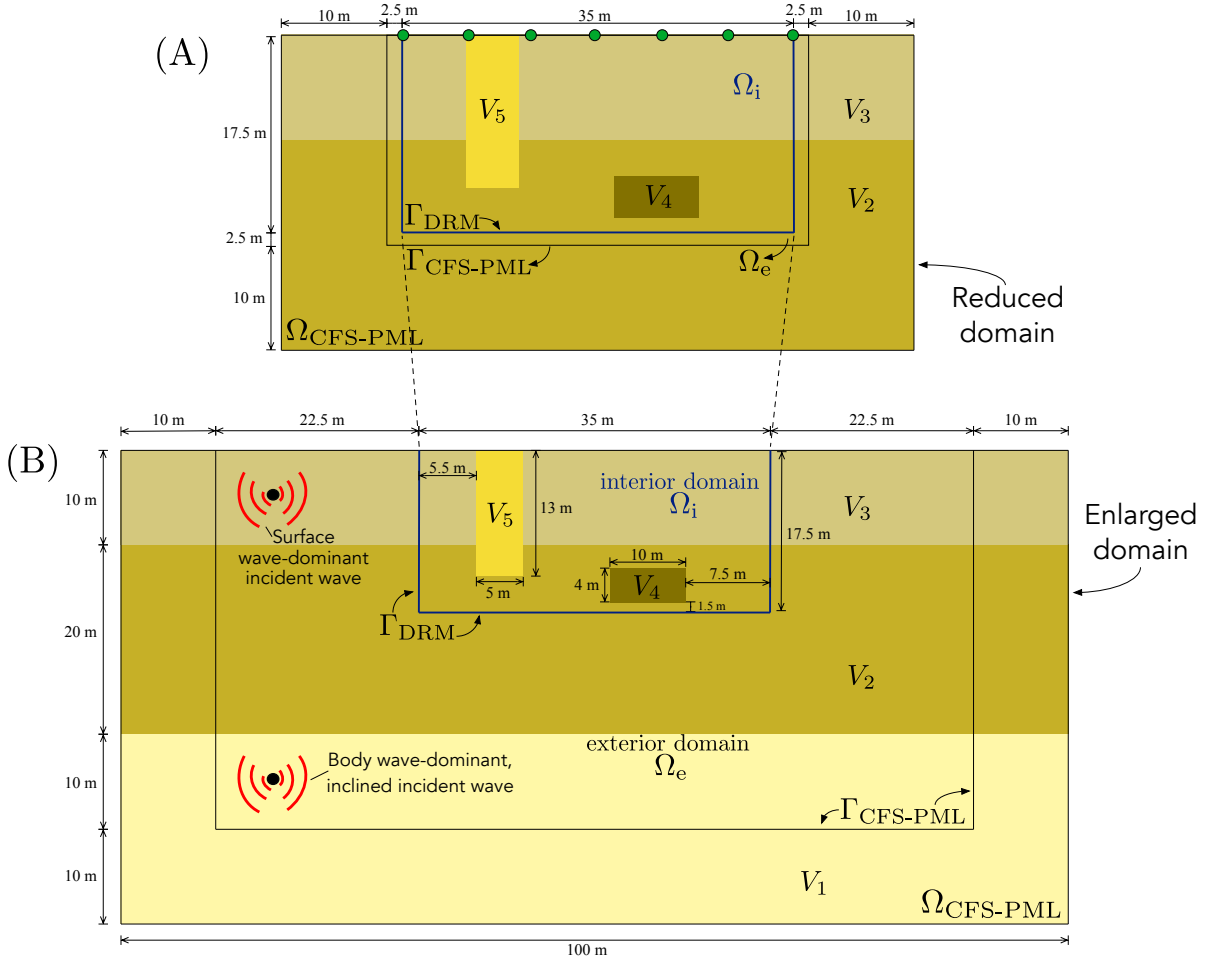

Figure 4: Computational models for the numerical experiments; (A) Reduced computational model used in inversion; (B) Enlarged computational model used for synthetic sensor data generation.

Both the reduced and the enlarged domains are heterogeneous; moreover, in addition to the layering, two stiff inclusions are also embedded within the reduced domain (Fig. 4). The properties of the various materials implicated in the model are as follows: the shear wave speeds are $V_{s_1} = 200$ m/s, $V_{s_2} = 150$ m/s, $V_{s_3} = 100$ m/s, $V_{s_4} = 500$ m/s, and $V_{s_5} = 800$ m/s; the dilatational wave speeds are $V_{p_1} = 400$ m/s, $V_{p_2} = 300$ m/s, $V_{p_3} = 200$ m/s, $V_{p_4} = 1000$ m/s, and $V_{p_5} = 1600$ m/s; and the mass density of both the reduced and enlarged domains is uniform and set at 1500 kg/m³.

We note that the properties of the reduced domain are considered *a priori* known; in practice, they could be

obtained via site characterization (e.g., spectral analysis of surface waves (SASW) method [27–31], multi-channel analysis of surface waves (MASW) method [32, 33], or full-waveform inversion (FWI) method [34–36]).

For the spatial discretization of the computational domains, we use a structured mesh, consisting of 9-noded quadrilateral elements with an edge size equal to 1 m, thus resulting in nodal spacing of 0.5 m. Given that the smallest shear wave velocity in our model is 100 m/s, and the highest dominant frequency is 10 Hz, there result about 20 nodes per the shortest wavelength, which is in line with typical recommendations for wave propagation problems.

For the temporal discretization, a time step size of 0.001 s, and a total observation time of 1.5 s are used in all numerical experiments. The spacing of the ground surface sensors is not fixed, but varies in our numerical experiments in order to study the effect of the sensor array density on the reconstructed wavefield; the first sensor is always situated at the top-left corner of Γ_{DRM}, while the last one is located at the top-right corner of Γ_{DRM}[6].

Without loss of generality, we use point body forces in the enlarged domain to generate the incident fields. A point source serves as a surrogate for a seismic source (e.g., seismic moment tensor at a fault), and results in generating both compressional and shear waves. To address the time dependence of the point sources, we use Ricker wavelets with a peak amplitude of 100 N/m and a central frequency of 2 Hz, 5 Hz, or 10 Hz to drive the vertical body force component $P_y(t)$, while the horizontal component $P_x(t)$ is set to zero. We remark that the presented method can accommodate any profile (spatial or temporal) of a seismic source in the enlarged domain; moreover, our inversion solver does not need to be informed of the profile of the source.

In order to assess the quality of the reconstructed total wavefield within Ω_i, we define a global space-time normalized error norm in the least-squares sense, per:

$$\mathcal{E}^{|\mathbf{u}|} = \frac{\sum_{j=1}^{N} |\mathbf{d}_j^{\text{target}} - \mathbf{d}_j^{\text{inv}}|^2}{\sum_{j=1}^{N} |\mathbf{d}_j^{\text{target}}|^2} \times 100[\%], \tag{12}$$

where $\mathbf{d}_j^{\text{target}}$ is the vector of the displacement amplitudes of the true total wavefield $|\mathbf{u}_i|$ of all nodes in Ω_i at the j-th time step; $\mathbf{d}_j^{\text{inv}}$ is its reconstructed counterpart induced by the inverted DRM forces $\hat{\mathbf{F}}_{\text{DRM}}^{\text{inv}}$; and N is the total number of time steps. Global norms $\mathcal{E}^{u_x}$ and $\mathcal{E}^{u_y}$ for the horizontal and vertical displacement components, respectively, are similarly defined.

5.1. Example 1: Inverting for the seismic forces and the total wavefield due to a body-wave-dominant seismic source

In this example, we study the performance of the presented approach when the near-surface deposits are excited by a body-wave-dominant source situated at the bottom-left of the enlarged domain. The source is a Ricker pulse with a central frequency of 10 Hz.

Figure 5 shows a snapshot of the target displacement amplitudes of the total wavefield taken at $t = 0.40$ s. The dashed line in the enlarged domain is $\Gamma_{\text{CFS-PML}}$, i.e., the interface between the enlarged domain and its surrounding CFS-PML buffer, while the solid line is the DRM boundary Γ_{DRM}, surrounding Ω_i. The total wavefield within Ω_i is shown in Fig. 5(A) and represents the target wavefield that the presented inversion approach ultimately seeks to reconstruct by using $\hat{\mathbf{F}}_{\text{DRM}}^{\text{inv}}$.

[6]Placing sensors at the intersection of the DRM with the ground surface is not required; it is merely convenient for the computational simulations.

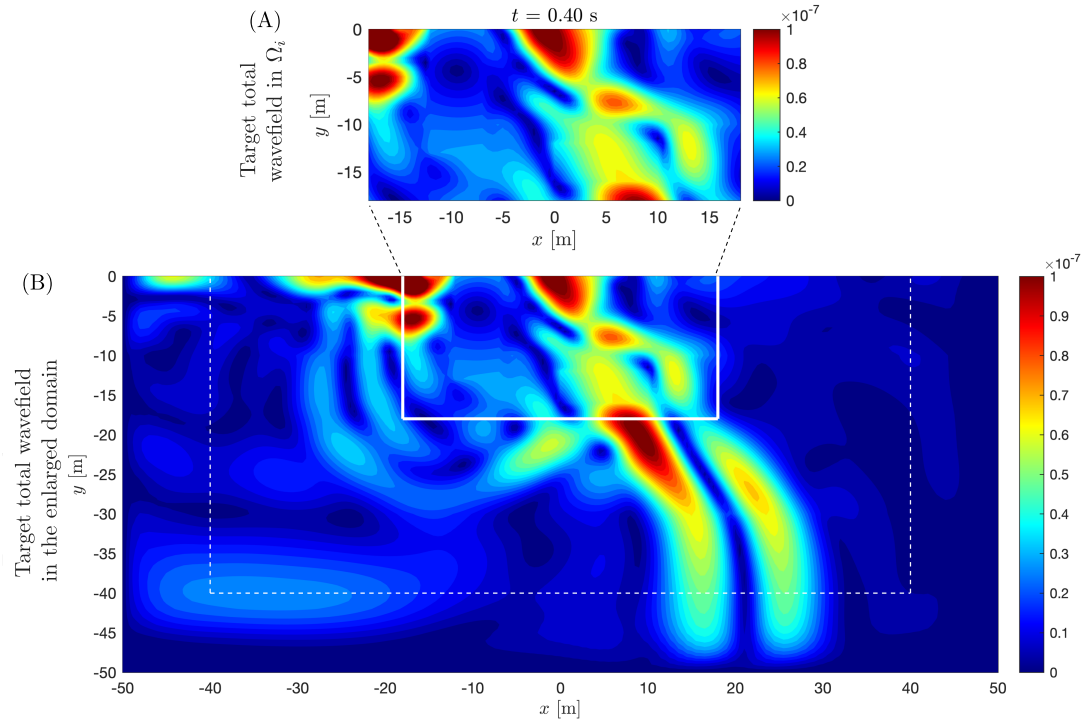

Figure 5: Example 1: Snapshot at $t = 0.40$ s of the total wavefield amplitudes induced by a body-wave-dominant source in the form of a body force Ricker pulse operating at 10 Hz. (A) Target total wavefield motion amplitudes $|\mathbf{u}_i|$ in Ω_i; (B) Total wavefield motion amplitudes in the enlarged domain.

To drive the inversion, we deploy 19 ground sensors spaced 2 m apart; thus, the sensor array extends over the entire surface of the reduced computational domain. Figure 6 compares the snapshots of the displacement amplitudes of target total wavefield in Ω_i that are computed using the enlarged domain solver against their reconstructed counterparts induced by the inverted DRM forces $\hat{\mathbf{F}}^{\text{inv}}_{\text{DRM}}$, after 500 inversion iterations. As can be seen, the reconstructed wavefields are, overall, in great agreement with the target wavefields, especially near the ground surface, with the accuracy somewhat degrading as the DRM boundary is approached. For example, if one were to consider the bottom half of the domain (i.e., -18 m$< y \leq$ -9 m), the associated error $\mathcal{E}^{|\mathbf{u}|}$ is 10.11%, while the error reduces to 1.04% when considering the top half of the domain (i.e., -9 m$< y \leq$ 0 m). This performance is as expected, since the vanishing of the misfit governs the error in the near-surface wavefields.

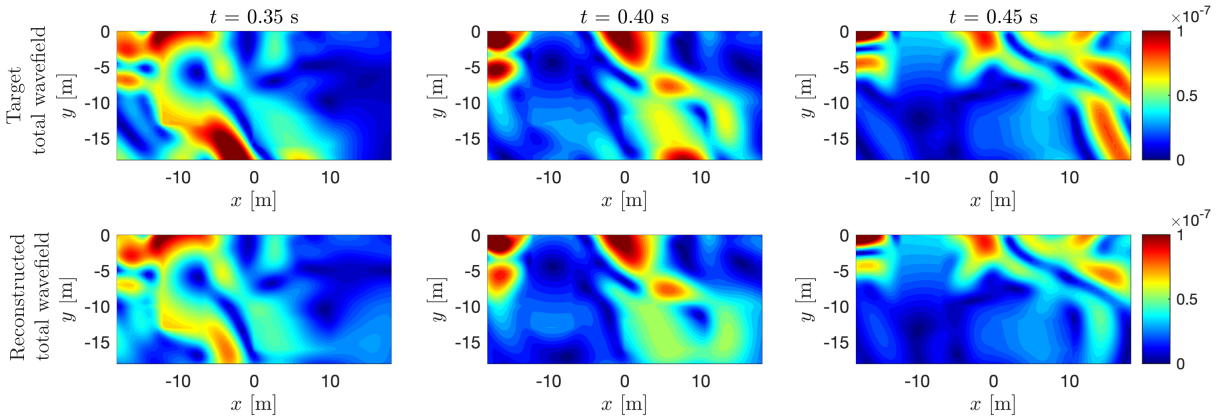

Figure 6: Example 1: (First row) Snapshots of the target displacement wavefield $|\mathbf{u}_i|$ in Ω_i induced by a body-wave-dominant source in the form of a body force Ricker pulse operating at 10 Hz; (Second row) reconstructed displacement wavefields induced by the inverted seismic DRM forces $\hat{\mathbf{F}}^{\text{inv}}_{\text{DRM}}$.

Figure 7 depicts the comparison of the target total wavefield in Ω_i and the reconstructed wavefield in terms of the acceleration amplitudes. As it can be seen, the reconstructed acceleration wavefields are in great agreement with their target counterparts. Similarly to the displacement wavefields, here too we observe better agreement within the top half of the domain than within the bottom half. Specifically, while the error $\mathcal{E}^{|\ddot{\mathbf{u}}|}$ is 1.50% within the top half of the domain, it increases to 11.47% within the bottom half of the domain. Furthermore, there is a slight worsening of the error associated with the acceleration fields (6.63%) when compared with the displacement fields (5.11%), but, overall, the accuracy is comparable.

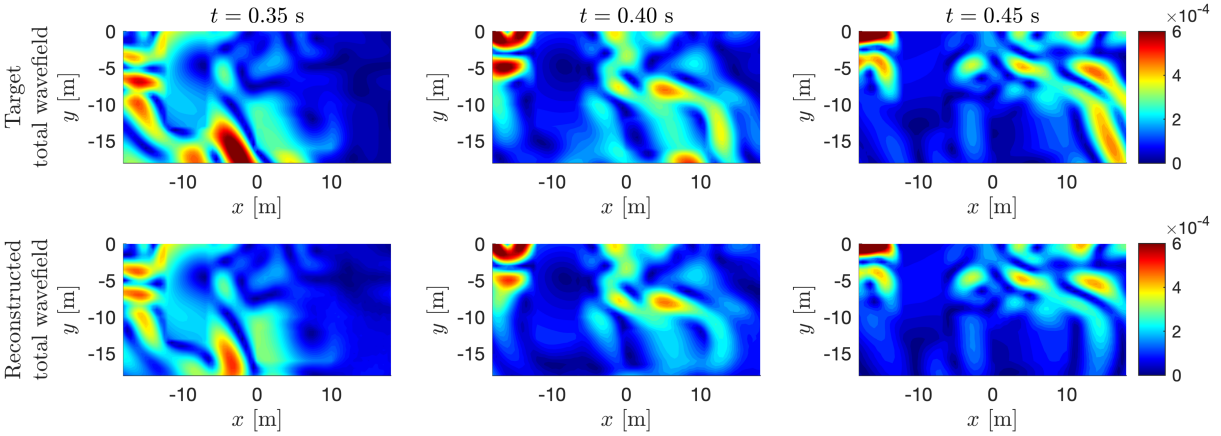

Figure 7: Example 1: (First row) Snapshots of the target wavefield $|\ddot{\mathbf{u}}_i|$ in Ω_i induced by a body-wave-dominant source in the form of a body force Ricker pulse operating at 10 Hz; (Second row) reconstructed acceleration wavefields induced by the inverted seismic DRM forces $\hat{\mathbf{F}}^{\text{inv}}_{\text{DRM}}$.

Figure 8 shows excellent agreement between the time-histories of the horizontal and vertical displacements of the measured ground motions and their reconstructed counterparts induced by $\hat{\mathbf{F}}^{\text{inv}}_{\text{DRM}}$ at the nineteen sensor locations on the ground surface; the excellent agreement is due to the successful minimization of the misfit functional.

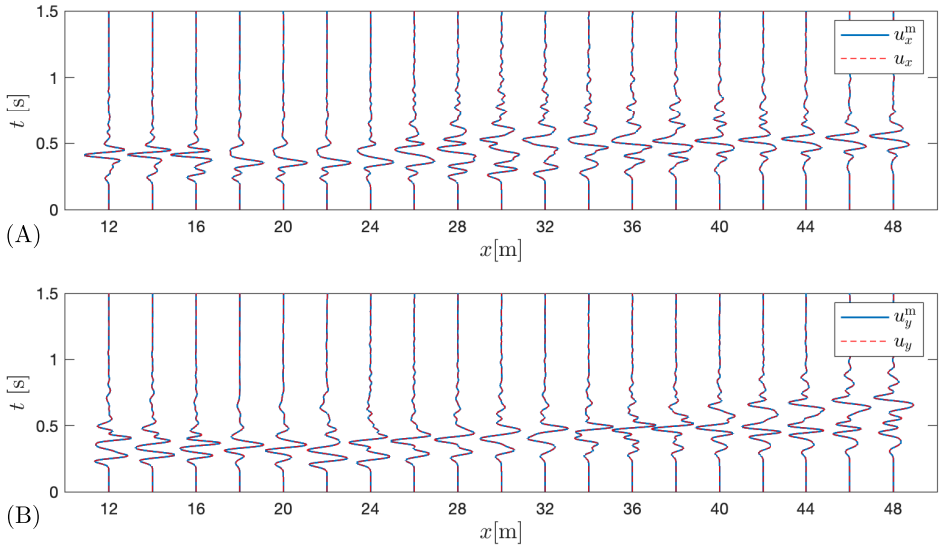

Figure 8: Example 1: Comparison between measured horizontal and vertical displacement time histories and their reconstructed counterparts induced by the inverted DRM forces $\hat{\mathbf{F}}_{\mathrm{DRM}}^{\mathrm{inv}}$ at 19 ground sensor locations.

Lastly, we are interested in the method's performance as the excitation's frequency content changes, and as the number and the spacing of the sensors changes. To this end, we consider three Ricker pulses driven by central frequencies of 2 Hz, 5 Hz, and 10 Hz, and different sensor spacing, varying between 1 m and 18 m. Table 1 tabulates the results for all cases considered.

Table 1: Summary of errors for various sensor array spacings and driving seismic source frequencies.

Case number	Central frequency	Sensor spacing	$\mathcal{E}^{\lvert\mathbf{u}\rvert}$	$\mathcal{E}^{u_x}$	$\mathcal{E}^{u_y}$
1.1	2 Hz	1 m	0.15%	0.68%	0.14%
1.2	2 Hz	2 m	0.14%	0.65%	0.14%
1.3	2 Hz	5 m	0.17%	0.76%	0.17%
1.4	2 Hz	7 m	0.19%	0.75%	0.18%
1.5	2 Hz	12 m	0.48%	4.39%	0.49%
1.6	2 Hz	18 m	1.05%	5.54%	1.55%
1.7	5 Hz	1 m	1.99%	3.95%	2.83%
1.8	5 Hz	2 m	1.90%	3.75%	2.67%
1.9	5 Hz	5 m	2.23%	4.22%	3.31%
1.10	5 Hz	7 m	2.56%	4.22%	4.53%
1.11	5 Hz	12 m	12.77%	21.69%	28.18%
1.12	10 Hz	1 m	5.21%	11.85%	7.04%
1.13	10 Hz	2 m	5.11%	11.70%	6.88%
1.14	10 Hz	5 m	7.92%	14.66%	11.53%
1.15	10 Hz	7 m	13.06%	19.84%	24.20%

Figure 9 illustrates the relationship between the error $\mathcal{E}^{|\mathbf{u}|}$ and both the dominant frequency of the source and the sensor spacing. As it can be seen, and as expected, the error increases as the density of the sensor array coarsens. Similarly, the error increases as the source frequency increases, but the error can be improved by increasing the mesh density. Overall, the error in the reconstructed total wavefields is remarkably low for all cases for which there is a sufficient, and relatively small, number of sensors deployed. Furthermore, the number of sensors per wavelength can serve as a criterion to establish the minimum sensor density required for a robust reconstruction of the seismic wavefield (i.e., $\mathcal{E}^{|\mathbf{u}|} \leq 10\%$). Per Fig. 9, it would be necessary to deploy at least 3 sensors per the shortest wavelength

(i.e., the shear wavelength in the upper layer of the domain). And, thus, for example, when using a source with a dominant frequency of 5 Hz (the shortest wavelength is 20 m), a sensor spacing of 12 m (about 1.67 sensors per wavelength) would not result in $\mathcal{E}^{|\mathbf{u}|} \leq 10\%$, but a sensor spacing of 7 m (about 2.9 sensors per wavelength) would satisfy the inequality.

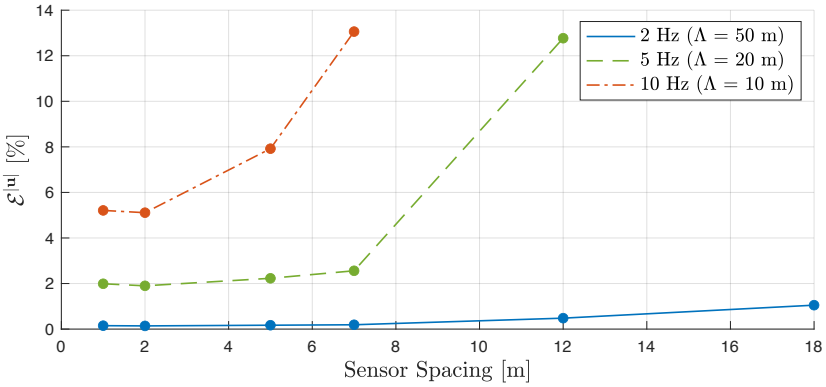

Figure 9: Relation of the error to the dominant frequency (or the shortest wavelength Λ) of the body-wave-dominant source and the sensor spacing (Example 1).

As discussed earlier, the inverted DRM forces, owing to the inherent multiplicity of *admissible* solutions, could generate strong scattered wavefields in the exterior domain Ω_e. Thus, having a quality absorbing condition at the truncation interface of the computational domain is of paramount importance in order to guard against pollution of the wavefield solutions from reflections off of the truncation boundary. To demonstrate the importance the CFS-PML buffer plays in obtaining quality solutions, we, next, compare the target and reconstructed total wavefields for two different truncation strategies, one resting on the CFS-PML, and a second one that relies on simple dashpots, commonly referred to as the Lysmer and Kuhlemeyer absorbing boundary condition [37]. We use the data of case 1.13 (see Table 1) to highlight the differences. The dashpot conditions are realized via:

$$\sigma_{xx} = \rho V_{\mathrm{p}} \dot{u}_x, \quad \sigma_{xy} = \rho V_{\mathrm{s}} \dot{u}_y, \qquad \text{on } \Gamma_{\mathrm{DRM}_{\mathrm{left}}} \text{ and } \Gamma_{\mathrm{DRM}_{\mathrm{right}}}, \tag{13}$$

$$\sigma_{xy} = \rho V_{\mathrm{s}} \dot{u}_x, \quad \sigma_{yy} = \rho V_{\mathrm{p}} \dot{u}_y, \qquad \text{on } \Gamma_{\mathrm{DRM}_{\mathrm{bottom}}}. \tag{14}$$

Figure 10 depicts snapshots of the target total wavefield $|\mathbf{u}_i|$ in Ω_i (top row), of the reconstructed total wavefield when the CFS-PML is used (middle row), and of the reconstructed total wavefield when the dashpot condition is used (bottom row). Moreover, Table 2 summarizes various global error metrics between the target and reconstructed total wavefields in Ω_i. From both Fig. 10 and Table 2, it is clear that the use of the dashpots severely degrades the quality of the reconstructed wavefields, and its use should be avoided.

Table 2: Errors in the reconstructed total wavefields obtained when using the CFS-PML versus the Lysmer and Kuhlemeyer absorbing boundary condition.

Truncation condition	$\mathcal{E}^{\lvert\mathbf{u}\rvert}$	$\mathcal{E}^{u_x}$	$\mathcal{E}^{u_y}$
CFS-PML by François et al. [16, 17]	5.11%	11.70%	6.88%
Lysmer and Kuhlemeyer [37]	11.51%	20.03%	19.54%

5.2. *Example 2: The effect of a structure*

In this example, we study the effect the addition of a structure within the domain of interest may have on the ability of the inversion algorithm to reconstruct the DRM seismic forces and the total wavefield within Ω_i (Fig. 11). The structure is modeled as a solid, partially buried, and partially extending above the ground surface: we set its shear and dilatational wave speeds at V_{s_6} = 3250 m/s and V_{p_6} = 5900 m/s, respectively. The target total wavefield is again induced by the body force of Example 1, operating at central frequencies of 5 Hz and 10 Hz. We also compare the

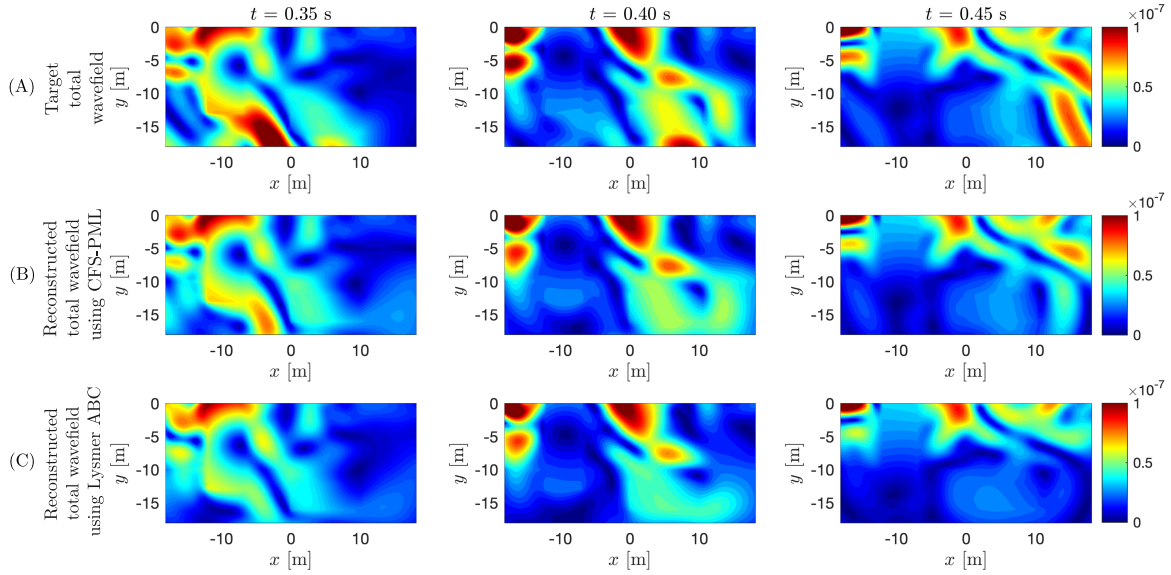

Figure 10: Example 1: (A) Target total wavefield $|\mathbf{u}_i|$ in Ω_i; and (B,C) reconstructed total wavefields obtained using the CFS-PML, and the Lysmer and Kuhlemeyer absorbing boundary condition, respectively.

performance of the inversion when (*i*) sensors are distributed on the ground surface with a 2 m spacing; and (*ii*) when additional 5 sensors are vertically deployed along the height of the structure, as shown in Fig. 11.

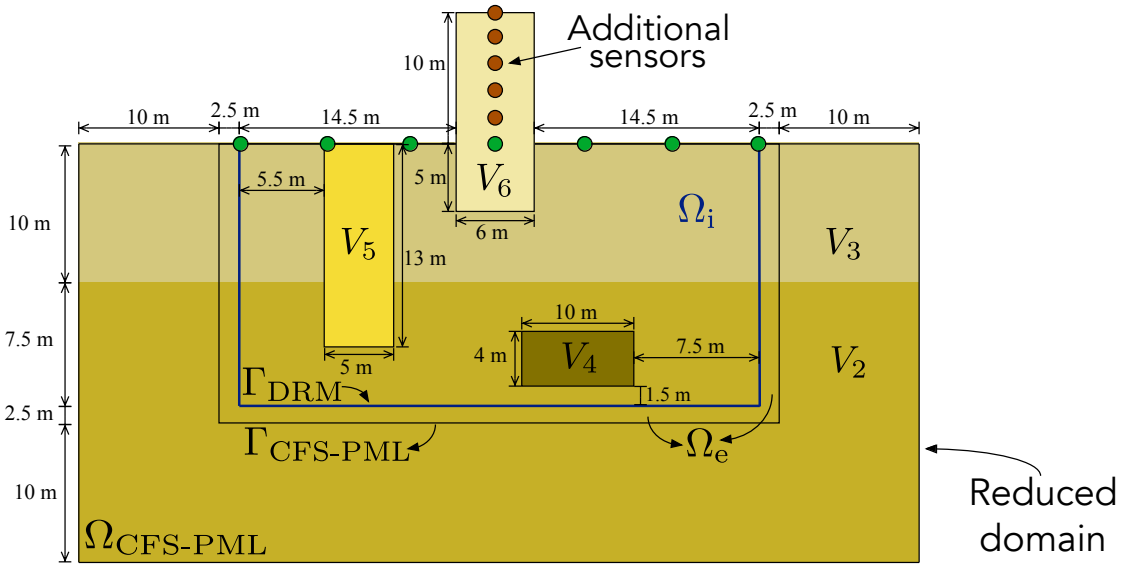

Figure 11: Computational model of the near-surface deposits, encompassing a structure.

We note that structure V_6 exhibits strong resonance at, approximately, 1.9 Hz, as depicted in Fig. 12. Specifically, Fig. 12 shows the maximum displacement amplitude of the topmost node of V_6, for frequencies ranging from 0.1 Hz to 15 Hz. Therefore, the structure's dominant amplification frequency is contained within the spectrum of the Ricker source, though not coinciding with the Ricker's central frequency (5Hz or 10Hz for the two cases considered).

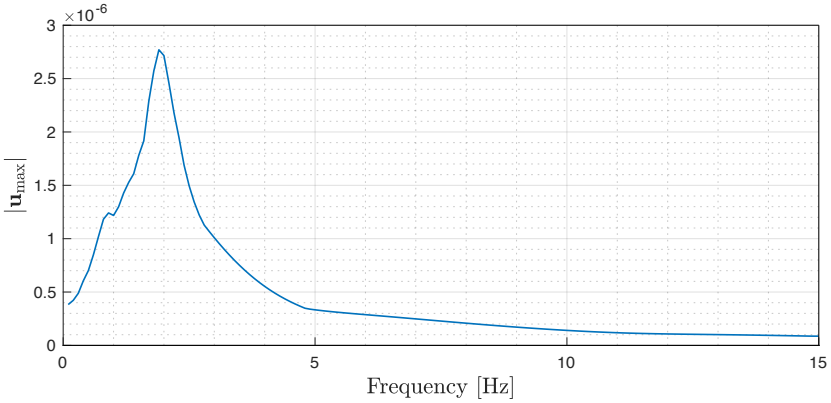

Figure 12: Maximum displacement amplitude $|\mathbf{u}_{\max}|$ of the topmost node of structure V_6 as a function of excitation frequency.

Table 3 shows the global error in the reconstructed total wavefields in Ω_i for four different cases after 500 iterations. The results show that the presented method can accurately estimate the wave motions in Ω_i, even in the presence of a structure: the error in the motion amplitudes $\mathcal{E}^{|\mathbf{u}|}$ is smaller than 10% in all cases.

Table 3: Example 2: Summary of errors in the total wavefield for two different sensor array configurations and two driving seismic source frequencies.

Case number	Central frequency	Sensors in the structure	Number of sensors	$\mathcal{E}^{\lvert\mathbf{u}\rvert}$	$\mathcal{E}^{u_x}$	$\mathcal{E}^{u_y}$
2.1A	5 Hz	No	19	2.75%	5.11%	5.11%
2.1B	5 Hz	Yes	19 + 5	3.60%	7.03%	6.66%
2.2A	10 Hz	No	19	8.73%	14.26%	13.84%
2.2B	10 Hz	Yes	19 + 5	9.78%	15.40%	16.05%

Table 3 also shows that the final values of $\mathcal{E}^{|\mathbf{u}|}$ for all Cases 2.1A to 2.2B[7], obtained by using only the distributed sensors on the top surface, are close to those obtained by using a combination of sensors on the ground surface and in the structure. Namely, the $\mathcal{E}^{|\mathbf{u}|}$ value of 2.75% of Case 2.1A (5 Hz without the vertical array) is close to the $\mathcal{E}^{|\mathbf{u}|}$ value of 3.06% of Case 2.1B (5 Hz with the vertical array), and the $\mathcal{E}^{|\mathbf{u}|}$ value of 8.73% of Case 2.2A (10 Hz without the vertical array) is close to the $\mathcal{E}^{|\mathbf{u}|}$ value of 9.78% of Case 2.2B (10 Hz with the vertical array).

Furthermore, Table 4 shows the global error in the reconstructed wavefields in the soil and in the structure, respectively. It can be seen that minimizing the misfit that includes the measurements on the vertical array of the structure makes the error $\mathcal{E}^{|\mathbf{u}|}$ in the soil to be greater than otherwise (e.g., 3.61% in Case 2.1A versus 4.75% in Case 2.1B). On the other hand, because the error $\mathcal{E}^{|\mathbf{u}|}$ in the structure is already quite small even when the vertical array is not used, we do not notice significant improvement of $\mathcal{E}^{|\mathbf{u}|}$ in the structure when its sensor array is used (i.e., 0.02% in Case 2.1A $\rightarrow$ 0.01% in Case 2.1B, and 0.38% in Case 2.2A $\rightarrow$ 0.38% in Case 2.2B). Thus, it seems that we may not need sensors in the structure for the presented algorithm, at least in this example with a single structure of a simple shape.

Table 4: Example 2: Summary of errors in the total wavefield in the soil and in the structure for two different driving seismic source frequencies and two different sensor array configurations.

Case	$\mathcal{E}^{\lvert\mathbf{u}\rvert}$	$\mathcal{E}^{\lvert\mathbf{u}\rvert}_{\text{soil}}$	$\mathcal{E}^{\lvert\mathbf{u}\rvert}_{\text{struct}}$	$\mathcal{E}^{u_x}$	$\mathcal{E}^{u_x}_{\text{soil}}$	$\mathcal{E}^{u_x}_{\text{struct}}$	$\mathcal{E}^{u_y}$	$\mathcal{E}^{u_y}_{\text{soil}}$	$\mathcal{E}^{u_y}_{\text{struct}}$
2.1A	2.75%	3.61%	0.02%	5.11%	6.61%	0.02%	5.11%	6.56%	0.01%
2.1B	3.60%	4.75%	0.01%	7.03%	9.12%	0.01%	6.66%	8.57%	0.01%
2.2A	8.73%	9.08%	0.38%	14.26%	14.69%	0.08%	13.84%	14.58%	0.89%
2.2B	9.78%	10.18%	0.38%	15.40%	15.85%	0.07%	16.05%	16.91%	0.89%

[7]Case 2.1A and 2.2A do not use measurement data from the vertical array in the structure, whereas Case 2.1B and 2.2B do.

Lastly, Fig. 13 shows snapshots of $|\mathbf{u}_i|$ of the target total wavefield in Ω_i and their estimated counterparts, for Case 2.1A (5 Hz central Ricker pulse frequency, and ground surface array only). Similarly, figures 14 and 15 show the snapshots of the target horizontal and vertical displacements and their reconstructed counterparts, respectively. Figures 13, 14, and 15 all indicate that the wavefields close to the lower DRM boundary are not as accurately reconstructed as those near the ground surface. Specifically, the error $\mathcal{E}^{|\mathbf{u}|}$ for the bottom half of the domain (i.e., -18 m< $y \leq$ -9 m) is 7.99%, while $\mathcal{E}^{|\mathbf{u}|}$ is only 0.38% for the near-surface wavefields (i.e., -9 m < $y \leq$ 0 m) and the wavefield in the structure. We suggest that, since the sensors are located at the upper part of the domain, the minimization of the misfit functional leads to more effective reconstruction of waves in the upper part of the domain than in the lower part.

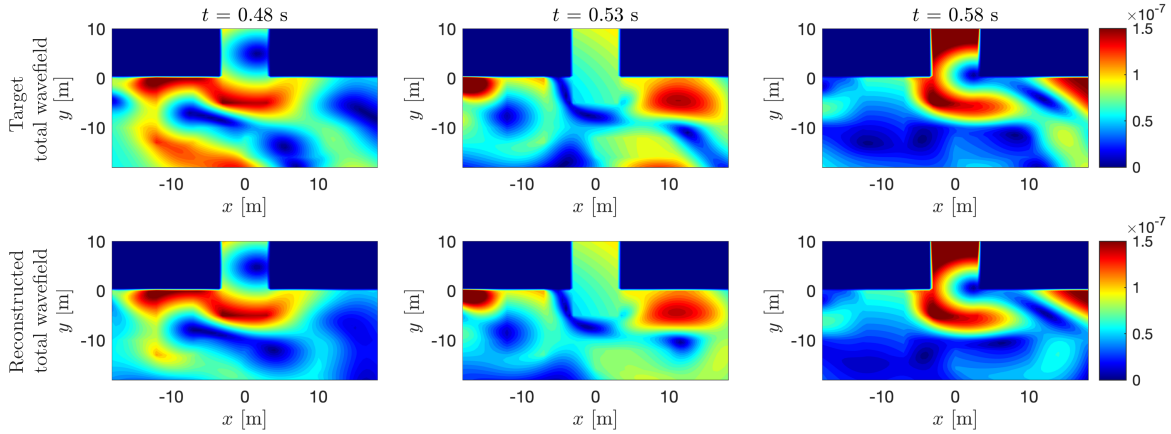

Figure 13: Example 2: Case 2.1A (without structure sensor array); (First row) Snapshots of the target wavefield $|\mathbf{u}_i|$ in Ω_i induced by a body-wave-dominant source in the form of a body force Ricker pulse operating at 5 Hz; (Second row) reconstructed wavefields induced by the inverted seismic DRM forces $\hat{\mathbf{F}}^{\text{inv}}_{\text{DRM}}$.

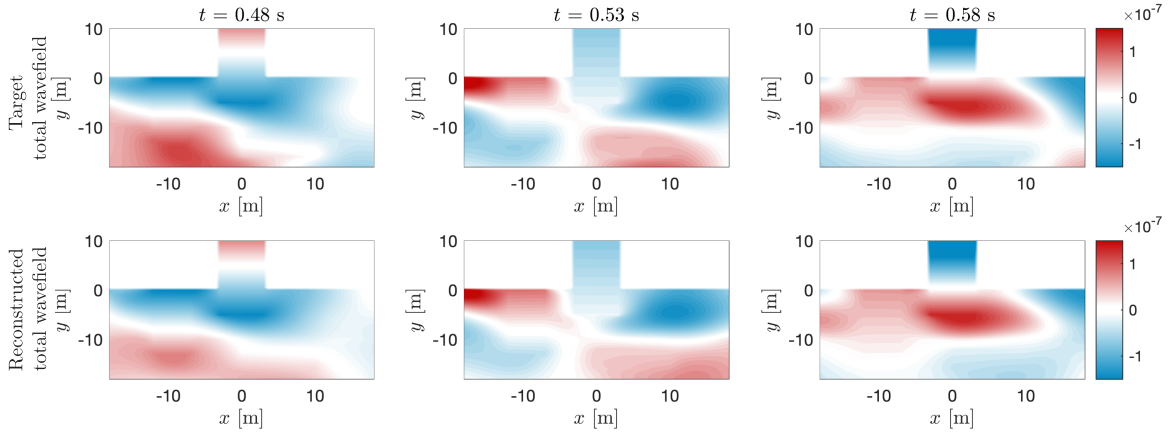

Figure 14: Example 2: Case 2.1A (without structure sensor array); (First row) Snapshots of the target horizontal component of the wavefield $|\mathbf{u}_i|$ in Ω_i induced by a body-wave-dominant source in the form of a body force Ricker pulse operating at 5 Hz; (Second row) reconstructed wavefields induced by the inverted seismic DRM forces $\hat{\mathbf{F}}^{\text{inv}}_{\text{DRM}}$.

5.3. Example 3: Inverting for the seismic forces and the total wavefield due to a surface-wave-dominant seismic source in the presence of a structure

In this example, we study the effect a surface-wave-dominant source has on the quality of the reconstructed total wavefields. In particular, the incident wave originates from a source embedded within the top-left area of the enlarged domain. We obtain results again for four different cases, corresponding to two different Ricker pulses with central frequencies of 5 Hz and 10 Hz, while we also consider two different array configurations, with and without a vertical sensor array in the structure.

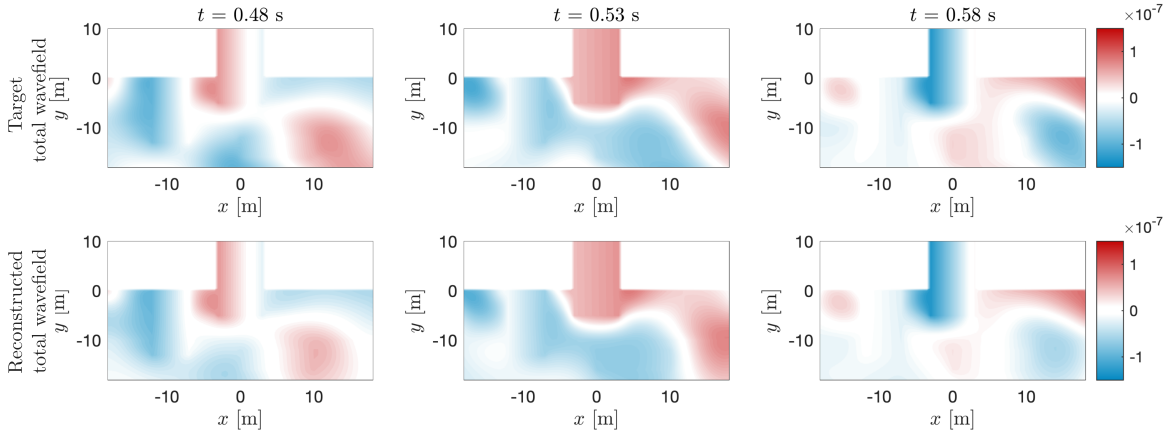

Figure 15: Example 2: Case 2.1A (without structure sensor array); (First row) Snapshots of the target vertical component of the wavefield $|\mathbf{u}_i|$ in Ω_i induced by a body-wave-dominant source in the form of a body force Ricker pulse operating at 5 Hz; (Second row) reconstructed wavefields induced by the inverted seismic DRM forces $\hat{\mathbf{F}}^{\text{inv}}_{\text{DRM}}$.

Table 5 shows the errors for all four cases (Cases 3.1A to 3.2B) after 500 inversion iterations. We note the relatively small errors, ranging from 0.34% to 3.83%, which demonstrate the successful reconstruction of the total wavefields induced by surface wave-dominant incident waves.

Table 5: Summary of errors in the total wavefield for two different array configurations and two driving seismic source frequencies

Case number	Central frequency	Sensors in the structure	Number of sensors	$\mathcal{E}^{\lvert\mathbf{u}\rvert}$	$\mathcal{E}^{u_x}$	$\mathcal{E}^{u_y}$
3.1A	5 Hz	No	19	0.34%	1.20%	0.39%
3.1B	5 Hz	Yes	19+5	0.47%	1.79%	0.53%
3.2A	10 Hz	No	19	3.41%	10.31%	5.13%
3.2B	10 Hz	Yes	19+5	3.83%	11.47%	5.90%

Table 5 also shows that the inclusion of the vertical sensor array in the structure did not significantly affect the resulting errors. Moreover, it can also be seen that when increasing the frequency of the incident waves, the errors increase. We also note that the errors $\mathcal{E}^{|\mathbf{u}|}$ for the surface-wave-dominant cases of Example 3 (range: 0.34% to 3.83%) were smaller than the errors reported in Example 2 (range: 2.75% to 9.78%), which pertained to the body-wave-dominant excitation. In general, the wavefield is better reconstructed in areas close to the ground surface sensor network, for both P-SV dominant incidence and for surface-wave-dominant incident motion, likely owing to the implications of the Cauchy-Kovalevskaya theorem, as previously discussed. The results are better for surface-wave-dominant incident motion, because the reconstruction also benefits from the fact that most of the motion is contained within the zone proximal to the sensors: the rise of the error at depth, which is expected, is over smaller amplitude wavefields, and has a lesser impact on the global error metric.

Figure 16 depicts snapshots of the target and reconstructed total wavefields $|\mathbf{u}_i|$ in Ω_i in Case 3.1A, i.e., when a Ricker wavelet with a 5 Hz dominant frequency is used as the source, and only the sensors on the ground surface are used for inversion. Figures 17 and 18 show snapshots of the target horizontal and vertical wavefield components, and their reconstructed counterparts, respectively, and as previously noted, they indicate a fairly satisfactory wavefield reconstruction.

5.4. Example 4: The effect of material property uncertainty

The inversion procedure outlined in this study relies on a priori estimates of the material properties of the near-surface deposits. It is important to acknowledge that in real-world scenarios, the actual properties of the near-surface deposits might diverge from their estimates. In this example, we attempt to assess the effect of such discrepancies between estimated and actual properties on the accuracy of the reconstructed wavefields.

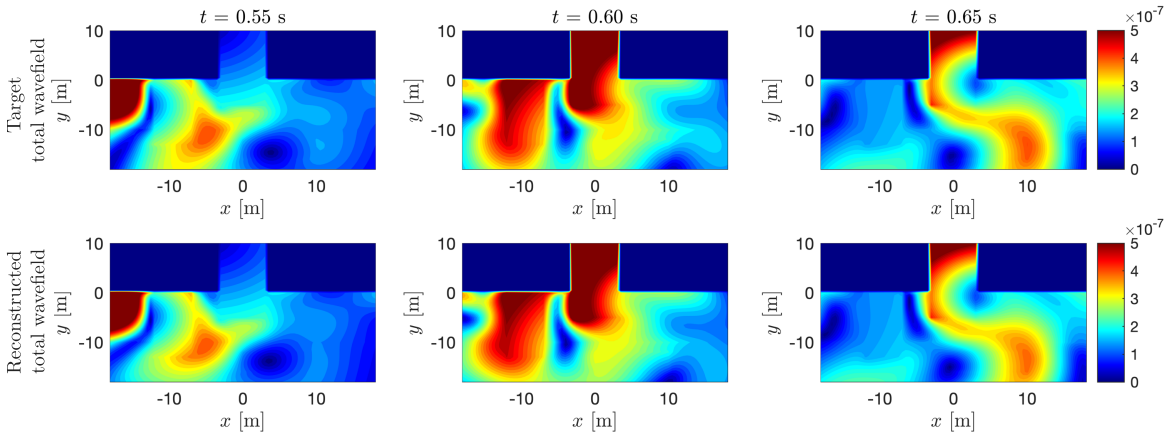

Figure 16: Example 3: Case 3.1A (without structure sensor array); (First row) Snapshots of the target wavefield $|\mathbf{u}_i|$ in Ω_i induced by a surface-wave-dominant source in the form of a body force Ricker pulse operating at 5 Hz; (Second row) reconstructed wavefields induced by the inverted seismic DRM forces $\hat{\mathbf{F}}^{\text{inv}}_{\text{DRM}}$.

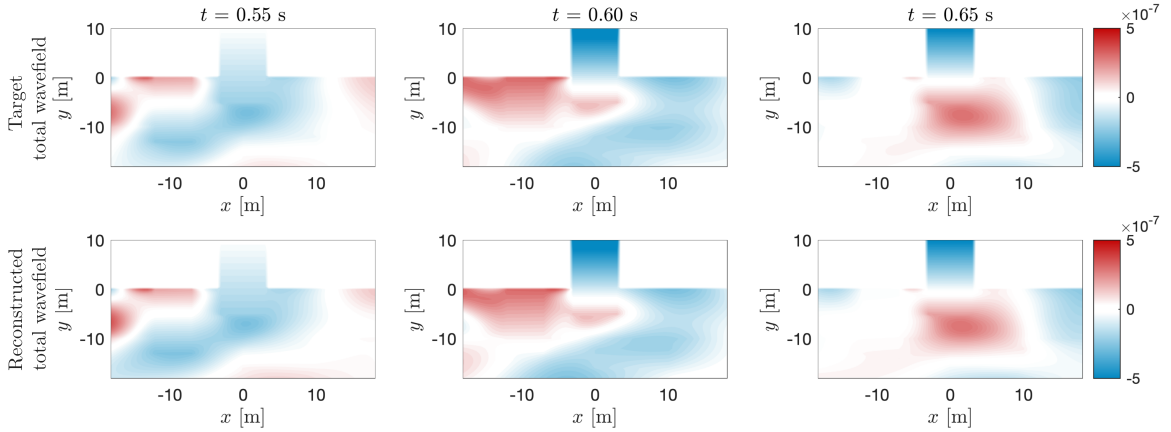

Figure 17: Example 3: Case 3.1A (without structure sensor array); (First row) Snapshots of the target horizontal component of the wavefield $|\mathbf{u}_i|$ in Ω_i induced by a surface-wave-dominant source in the form of a body force Ricker pulse operating at 5 Hz; (Second row) reconstructed wavefields induced by the inverted seismic DRM forces $\hat{\mathbf{F}}^{\text{inv}}_{\text{DRM}}$.

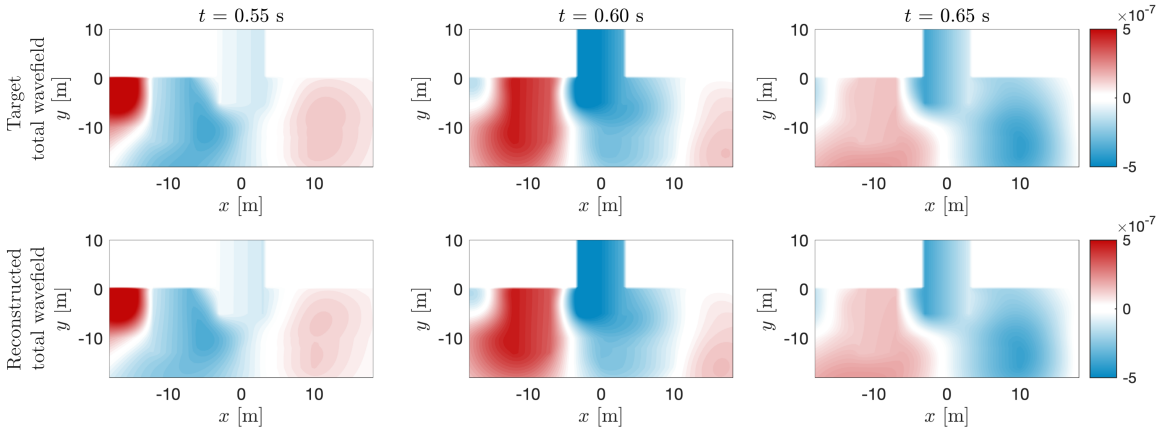

Figure 18: Example 3: Case 3.1A (without structure sensor array); (First row) Snapshots of the target vertical component of the wavefield $|\mathbf{u}_i|$ in Ω_i induced by a surface-wave-dominant source in the form of a body force Ricker pulse operating at 5 Hz; (Second row) reconstructed wavefields induced by the inverted seismic DRM forces $\hat{\mathbf{F}}^{\text{inv}}_{\text{DRM}}$.

To this end, we use again the same setup that was used in the previous numerical experiments (Fig. 11), with the following modifications: here, we assume that the previously used material properties correspond to estimates that differ from their true values by 2% to 5% as shown in Table 6. In addition, we also assume that the true depth of the topmost layer is 9 m, whereas the estimated depth was 10 m. We note that the sensor data were obtained using the true/actual values, and not the estimated values.

Table 6: Summary of the shear and dilatational wave speeds used in Example 4

Wave	Estimated properties		True properties (2% deviation)		True properties (5% deviation)	
speed (m/s)	V_s	V_p	V_s	V_p	V_s	V_p
V_2	150	300	147	294	142.5	285
V_3	100	200	102	204	105	210
V_4	500	1000	510	1020	525	1050
V_5	800	1600	784	1568	760	1520
V_6	3250	5900	3185	5782	3087.5	5605

We study four different cases, corresponding to two different Ricker pulses with central frequencies of 5 Hz and 10 Hz and two different property distributions, exhibiting 2% and 5% deviations from the estimated properties, respectively. Table 7 shows the error between the reconstructed and true wavefields for all four cases, denoted as Cases 4.1A, 4.1B, 4.2A and 4.2B, respectively. Table 7 also includes the errors for Cases 2.1A and 2.2A, where no uncertainty was considered (Example 2), and are included here for reference. The results show that the error $\mathcal{E}^{|\mathbf{u}|}$ increases as the deviation from the true properties increases. Table 7 also shows that error worsens further with higher frequencies.

Table 7: Summary of errors for different levels of uncertainty in wave speeds and driving seismic source frequency

Case number	Central frequency	Uncertainty in in wave speeds	$\mathcal{E}^{\lvert\mathbf{u}\rvert}$	$\mathcal{E}^{u_x}$	$\mathcal{E}^{u_y}$
2.1A	5 Hz	0%	2.75%	5.11%	5.11%
4.1A	5 Hz	2%	3.79%	9.41%	6.10%
4.1B	5 Hz	5%	5.14%	13.83%	7.86%
2.2A	10 Hz	0%	8.73%	14.26%	13.84%
4.2A	10 Hz	2%	10.10%	18.96%	16.55%
4.2B	10 Hz	5%	11.99%	22.72%	20.81%

The top row of Fig. 19 shows snapshots of the true wavefields $|\mathbf{u}_i|$ in Ω_i when a 5 Hz central Ricker pulse frequency is employed. Furthermore, the second, third, and fourth row of Fig. 19 show the reconstructed wavefield for Cases 2.1A, 4.1A, and 4.1B, respectively, corresponding to 0%, 2%, and 5% uncertainty in wave speeds. Although, as depicted in Fig. 19, there is a gradual worsening of the reconstructed wavefields as the deviation between true and estimated properties becomes greater, it is noteworthy that the wavefields are still reasonably well reconstructed near the top of the domain.

6. Conclusions

We discussed a systematic methodology for reconstructing the total seismic wavefield within the near-surface deposits using scant ground-surface measurements, under the assumption that the deposits have been previously characterized. We assumed further the site to be arbitrarily heterogeneous, and that the incident seismic motion to induce deformations that remain within the linear range. The total wavefield reconstruction is of importance not only for assessing seismic risk in sites where the infrastructure has remained, by and large, unchanged over time, but also in sites where infrastructure modifications are planned.

To reconstruct the seismic wavefield everywhere within a site of interest, the presented methodology requires no prior knowledge of the seismic event or of the source characteristics. Instead, the method aims at the reconstruction

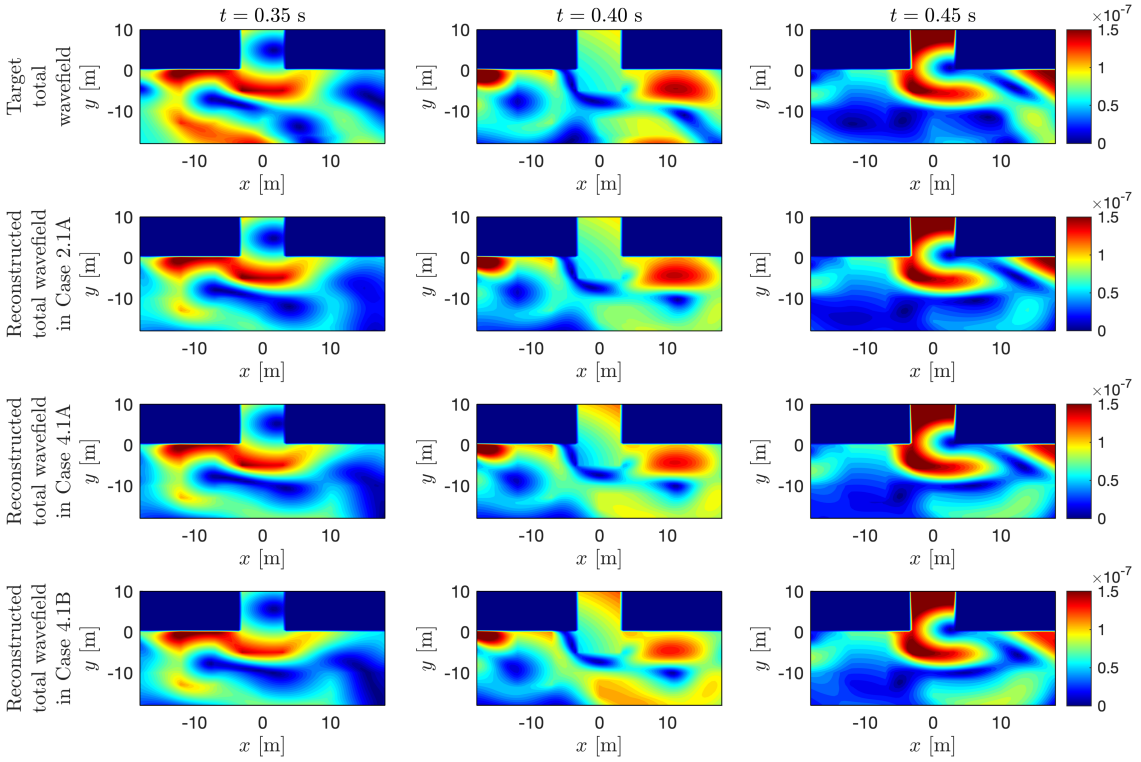

Figure 19: Example 4: (First row) Snapshots of the target wavefield $|\mathbf{u}_i|$ in Ω_i induced by a body-wave-dominant source operating at 5 Hz; (Second-Fourth row) reconstructed wavefields in Case 2.1A, 4.1A, and 4.1B, respectively, corresponding to 0%, 2%, and 5% uncertainty in wave speeds.

of seismic forces along the, so-called, DRM boundary, enveloping the near-surface deposits of interest. We discussed that there are infinitely many DRM force distributions that could satisfy the data, and argued that any single one of the DRM force distributions would result in the true total wavefield in the interior, but could result in strong (and non-physical) scattered motion in the domain exterior to the DRM boundary and the deposits of interest. To combat large amplitude scattered motion that may pollute the total wavefield in the domain of interest, we deployed a state-of-the-art absorptive CFS-PML buffer to force the decay of outgoing scattered waves within the buffer.

On the technical side, we cast the inverse source problem as a PDE-constrained optimization problem, where the PDE was incorporated as a constraint in its space-time discrete form. We used a gradient-based minimization scheme, powered by a discretize-then-optimize (DTO) approach, which aimed at minimizing the misfit between measured time-series of the total wavefield at the sensors and their reconstructed counterparts –the latter obtained from trial DRM seismic force distributions.

The following is a summary of observations from the numerical experiments.

- The inverted DRM forces reconstruct fairly well the total wavefield in the interior domain of interest, which may also include structures.
- The reconstructed total wavefield tends to be more accurate in the vicinity of the sensors than in depth.
- For quality reconstructions of the total wavefield, the required sensor spacing and density depend on the frequency content of the incident motion: higher frequency content demands denser arrays.
- The method is effective for arbitrarily incoherent incident fields; surface-wave-dominant incident fields tend to reconstruct the wavefield more accurately than body-wave-dominant fields.
- The method provides acceptable accuracy even in the presence of geophysical uncertainties. The results show that the error in the reconstructed wavefield increases with rising uncertainties, as would be expected, but the wavefields are reasonably well recovered in the topmost layers, proximal to the free surface and the sensor array.

We note that the presented methodology is readily scalable to three dimensions and, with a few modifications, could also accommodate nonlinear behavior in the interior domain

Acknowledgments

The work of the first and last authors was supported by the National Science Foundation under Award CMMI-2044887 and CMMI-2053694. Any opinions, findings, and conclusions or recommendations expressed in this material are those of the authors and do not necessarily reflect the views of the National Science Foundation. The last author is also grateful for a Faculty Research and Creative Endeavors (FRCE) Research Grant-48058 at Central Michigan University that partially supported this work.

Data Availability

Some or all data, models, or code generated or used during the study are available from the corresponding author by request.

Nomenclature

Symbol	Comment
Γ_{DRM} and Γ'_{DRM}	DRM layer boundaries
$\Gamma_{\text{CFS-PML}}$	Interface boundary between Ω_e and $\Omega_{\text{CFS-PML}}$
Ω_i, Ω_e	Interior and exterior domains, respectively
$\Omega_{\text{CFS-PML}}$	Perfectly-matched-layer wave-absorbing buffer
i, d, e	Subscripts for matrix and vector partitions in Ω_i, Γ_{DRM}, and Ω_e, respectively
$\mathbf{u}_i$, $\mathbf{u}_d$	Total displacement wavefields in Ω_i and on Γ_{DRM}, respectively
$\mathbf{u}^0$	Free-field motion
$\mathbf{w}_e$, $\boldsymbol{\vartheta}$, $\boldsymbol{\varphi}$, $\boldsymbol{\eta}$	Scattered displacement wavefield and three auxiliary fields within CFS-PML
$\mathbf{N}_u$, $\mathbf{N}_\vartheta$, $\mathbf{N}_\varphi$, $\mathbf{N}_\eta$	Shape functions for ($\mathbf{u}_i$, $\mathbf{u}_d$, $\mathbf{w}_e$), $\boldsymbol{\vartheta}$, $\boldsymbol{\varphi}$, and $\boldsymbol{\eta}$, respectively
$\mathbf{B}_x$, $\mathbf{B}_y$, $\mathbf{B}_\vartheta$, $\mathbf{B}_\varphi$	Shape function derivatives
$\mathbf{U}_i$, $\mathbf{U}_d$	Vectors of nodal values for $\mathbf{u}_i$ and $\mathbf{u}_d$, respectively
$\mathbf{W}_e$, $\boldsymbol{\Theta}$, $\boldsymbol{\Phi}$, $\mathbf{H}$	Vectors of nodal values for $\mathbf{w}_e$, $\boldsymbol{\vartheta}$, $\boldsymbol{\varphi}$, and $\boldsymbol{\eta}$, respectively
$\mathbf{U}$	Vector consisting of $\mathbf{U}_i$, $\mathbf{U}_d$, and $\mathbf{V}$
$\mathbf{V}$	Vector consisting of $\mathbf{W}_e$, $\boldsymbol{\Theta}$, $\boldsymbol{\Phi}$, and $\mathbf{H}$
$\hat{\mathbf{d}}$	Vector consisting of the time discretization of $\mathbf{U}(t)$, $\dot{\mathbf{U}}(t)$, and $\ddot{\mathbf{U}}(t)$ for all time steps
$\hat{\mathbf{d}}^{\text{m}}$	Vector consisting of measured responses
$\hat{\boldsymbol{\lambda}}$	Lagrange multiplier vector (space-time discrete)
$\hat{\mathbf{d}}^{\text{inv}}$	Vector consisting of computed (inverted) responses
$\mathbf{d}_j^{\text{target}}$	Vector of target $\lvert\mathbf{u}_i\rvert$ of all nodes in Ω_i at the j-th time step
$\mathbf{d}_j^{\text{inv}}$	Vector of reconstructed $\lvert\mathbf{u}_i\rvert$ induced by $\hat{\mathbf{F}}^{\text{inv}}_{\text{DRM}}$ of all nodes in Ω_i at the j-th time step
$\mathbf{P}_{\Gamma_{\text{DRM}}}$, $\mathbf{P}_{\Gamma'_{\text{DRM}}}$	Seismic forces on Γ_{DRM} and on Γ'_{DRM}, respectively
$\mathbf{F}_{\text{DRM}}$	Global seismic force vector
$\hat{\mathbf{F}}_{\text{DRM}}$	Time discretization of $\mathbf{F}_{\text{DRM}}(t)$ for all time steps
$\hat{\mathbf{F}}^{\text{inv}}_{\text{DRM}}$	Trial (inverted) distributions of the seismic forces $\hat{\mathbf{F}}_{\text{DRM}}$
$\mathbf{M}$, $\mathbf{K}$, $\mathbf{C}$	Global mass, stiffness, and damping matrices for $\Omega_i \cup \Omega_e \cup \Omega_{\text{CFS-PML}}$
$\mathbf{M}_{\text{PML}}$, $\mathbf{K}_{\text{PML}}$, $\mathbf{C}_{\text{PML}}$	Global mass, stiffness, and damping matrices for CFS-PML
$\mathbf{Q}$	Discrete space-time forward operator
$\hat{\mathcal{A}}$	Discrete objective functional
$\hat{\mathcal{L}}$	Discrete Lagrangian functional
$\mathbf{B}$, $\overline{\mathbf{B}}$	Block diagonal matrices with non-zero entries corresponding to sensor locations
$\mathcal{E}^{\lvert\mathbf{u}\rvert}$	Error norm for $\lvert\mathbf{u}_i\rvert$
$\mathcal{E}^{u_x}$	Error norm for the horizontal component of $\mathbf{u}_i$
$\mathcal{E}^{u_y}$	Error norm for the vertical component of $\mathbf{u}_i$
N_{s}	Number of sensors on the ground surface
N	Total number of time steps
τ	Final time step
V_{s}, V_{p}	Shear and dilatational wave speed
λ, μ	Lamé parameters
α_x, β_x, ω_x	Real and imaginary stretching functions and frequency shift in the x direction
α_y, β_y, ω_y	Real and imaginary stretching functions and frequency shift in the y direction

Appendix A. On the CFS-PML matrices $\mathbf{M}_{\mathrm{PML}}$, $\mathbf{C}_{\mathrm{PML}}$, and $\mathbf{K}_{\mathrm{PML}}$

The non-convolutional second-order Complex-Frequency-Shifted Perfectly-Matched-Layer [16, 17] is used for truncating the unbounded domain, following a mixed-field formulation. Within the PML, the scattered displacements $\mathbf{w}_e$, and the three auxiliary variables, $\boldsymbol{\vartheta}$, $\boldsymbol{\varphi}$ and $\boldsymbol{\eta}$, are discretized using:

$$\mathbf{w}_e(\mathbf{x},t) = \mathbf{N}_u(\mathbf{x})\,\mathbf{W}_e(t), \tag{A.1}$$

$$\boldsymbol{\vartheta}(\mathbf{x},t) = \mathbf{N}_\vartheta(\mathbf{x})\,\boldsymbol{\Theta}(t), \tag{A.2}$$

$$\boldsymbol{\varphi}(\mathbf{x},t) = \mathbf{N}_\varphi(\mathbf{x})\,\boldsymbol{\Phi}(t), \tag{A.3}$$

$$\boldsymbol{\eta}(\mathbf{x},t) = \mathbf{N}_\eta(\mathbf{x})\,\mathbf{H}(t), \tag{A.4}$$

where $\mathbf{N}_{(.)}$ are vectors of global basis functions. The PML matrices are defined as [16, 17]:

$$\mathbf{M}_{\mathrm{PML}} = \int_{\Omega_{\mathrm{CFS-PML}}} \begin{bmatrix} \rho A_2 \mathbf{N}_u^{\mathrm{T}}\mathbf{N}_u & \mathbf{0} & \mathbf{0} & \rho A_2 \mathbf{N}_u^{\mathrm{T}}\mathbf{N}_\eta \\ \mathbf{0} & \gamma_2 \mathbf{N}_\vartheta^{\mathrm{T}}\mathbf{N}_\vartheta & \mathbf{0} & \mathbf{0} \\ \mathbf{0} & \mathbf{0} & \delta_2 \mathbf{N}_\varphi^{\mathrm{T}}\mathbf{N}_\varphi & \mathbf{0} \\ \mathbf{0} & \mathbf{0} & \mathbf{0} & B_2 \mathbf{N}_\eta^{\mathrm{T}}\mathbf{N}_\eta \end{bmatrix} \mathrm{d}\Omega, \tag{A.5}$$

$$\mathbf{C}_{\mathrm{PML}} = \int_{\Omega_{\mathrm{CFS-PML}}} \begin{bmatrix} \rho A_1 \mathbf{N}_u^{\mathrm{T}}\mathbf{N}_u & \mathbf{0} & \mathbf{0} & \rho A_1 \mathbf{N}_u^{\mathrm{T}}\mathbf{N}_\eta \\ -\left(\delta_1 - \frac{\alpha_y}{\alpha_x}\gamma_1\right)\mathbf{N}_\vartheta^{\mathrm{T}}\mathbf{L}_\vartheta^{\mathrm{T}}\mathbf{B}_x & \gamma_1 \mathbf{N}_\vartheta^{\mathrm{T}}\mathbf{N}_\vartheta & \mathbf{0} & \mathbf{0} \\ -\left(\gamma_1 - \frac{\alpha_x}{\alpha_y}\delta_1\right)\mathbf{N}_\varphi^{\mathrm{T}}\mathbf{L}_\varphi^{\mathrm{T}}\mathbf{B}_y & \mathbf{0} & \delta_1 \mathbf{N}_\varphi^{\mathrm{T}}\mathbf{N}_\varphi & \mathbf{0} \\ B_1 \mathbf{N}_\eta^{\mathrm{T}}\mathbf{N}_u & \mathbf{0} & \mathbf{0} & B_1 \mathbf{N}_\eta^{\mathrm{T}}\mathbf{N}_\eta \end{bmatrix} \mathrm{d}\Omega, \tag{A.6}$$

$$\mathbf{K}_{\mathrm{PML}} = \int_{\Omega_{\mathrm{CFS-PML}}} \begin{bmatrix} \frac{\alpha_y}{\alpha_x}\mathbf{B}_x^{\mathrm{T}} C \mathbf{B}_x + \frac{\alpha_x}{\alpha_y}\mathbf{B}_y^{\mathrm{T}} C \mathbf{B}_y + \mathbf{B}_x^{\mathrm{T}} C \mathbf{B}_y + \mathbf{B}_y^{\mathrm{T}} C \mathbf{B}_x + \rho A_0 \mathbf{N}_u^{\mathrm{T}}\mathbf{N}_u & \mathbf{B}_x^{\mathrm{T}} C \mathbf{B}_\vartheta & \mathbf{B}_y^{\mathrm{T}} C \mathbf{B}_\varphi & \rho A_0 \mathbf{N}_u^{\mathrm{T}}\mathbf{N}_\eta \\ -\left(\delta_0 - \frac{\alpha_y}{\alpha_x}\gamma_0\right)\mathbf{N}_\vartheta^{\mathrm{T}}\mathbf{L}_\vartheta^{\mathrm{T}}\mathbf{B}_x & \gamma_0 \mathbf{N}_\vartheta^{\mathrm{T}}\mathbf{N}_\vartheta & \mathbf{0} & \mathbf{0} \\ -\left(\gamma_0 - \frac{\alpha_x}{\alpha_y}\delta_0\right)\mathbf{N}_\varphi^{\mathrm{T}}\mathbf{L}_\varphi^{\mathrm{T}}\mathbf{B}_y & \mathbf{0} & \delta_0 \mathbf{N}_\varphi^{\mathrm{T}}\mathbf{N}_\varphi & \mathbf{0} \\ B_0 \mathbf{N}_\eta^{\mathrm{T}}\mathbf{N}_u & \mathbf{0} & \mathbf{0} & B_0 \mathbf{N}_\eta^{\mathrm{T}}\mathbf{N}_\eta \end{bmatrix} \mathrm{d}\Omega. \tag{A.7}$$

In the above,

$$\mathbf{L}_\vartheta = \begin{bmatrix} 1 & 0 \\ 0 & 0 \\ 0 & 1 \end{bmatrix}, \quad \mathbf{L}_\varphi = \begin{bmatrix} 0 & 0 \\ 0 & 1 \\ 1 & 0 \end{bmatrix}, \quad C = \begin{bmatrix} \lambda + 2\mu & \lambda & 0 \\ \lambda & \lambda + 2\mu & 0 \\ 0 & 0 & \mu \end{bmatrix}, \tag{A.8}$$

$$A_0 = (\alpha_x\omega_x + \beta_x)\left(\alpha_y\omega_y + \beta_y\right), \quad A_1 = \alpha_x\left(\alpha_y\omega_y + \beta_y\right) + \alpha_y\left(\alpha_x\omega_x + \beta_x\right), \quad A_2 = \alpha_x\alpha_y, \tag{A.9}$$

$$B_0 = \omega_x\omega_y, \quad B_1 = \omega_x + \omega_y, \quad B_2 = 1, \tag{A.10}$$

$$\gamma_0 = (\alpha_x\omega_x + \beta_x)\,\omega_y, \quad \gamma_1 = \alpha_x\left(\omega_x + \omega_y\right) + \beta_x, \quad \gamma_2 = \alpha_x, \tag{A.11}$$

$$\delta_0 = \left(\alpha_y\omega_y + \beta_y\right)\omega_x, \quad \delta_1 = \alpha_y\left(\omega_x + \omega_y\right) + \beta_y, \quad \delta_2 = \alpha_y, \tag{A.12}$$

where λ and μ are the Lamé parameters; α_x, β_x are the real and the imaginary stretching parameters of the PML's stretching function, respectively, and ω_x is the frequency shift in the x direction; α_y, β_y, and ω_y are the corresponding quantities along the y direction. In addition, we define $\mathbf{B}_x = \mathbf{L}_x\mathbf{N}_u$, $\mathbf{B}_y = \mathbf{L}_y\mathbf{N}_u$, $\mathbf{B}_\vartheta = \mathbf{L}_\vartheta\mathbf{N}_\vartheta$, and $\mathbf{B}_\varphi = \mathbf{L}_\varphi\mathbf{N}_\varphi$, where

$$\mathbf{L}_x = \begin{bmatrix} \frac{\partial}{\partial x} & 0 \\ 0 & 0 \\ 0 & \frac{\partial}{\partial x} \end{bmatrix}, \quad \mathbf{L}_y = \begin{bmatrix} 0 & 0 \\ 0 & \frac{\partial}{\partial y} \\ \frac{\partial}{\partial y} & 0 \end{bmatrix}. \tag{A.13}$$

Appendix B. On the compact discrete operators $\mathbf{Q}$ and $\hat{\mathbf{d}}$ of (6)

The discrete forward operator $\mathbf{Q}$ results from the standard second-order semi-discrete equations of motion (3), following the introduction of the average acceleration implicit Newmark time-integration scheme. Specifically, it can be

shown that:

$$\mathbf{Q} = \begin{bmatrix} \mathbf{I} & 0 & 0 & 0 & 0 & 0 & \dots & 0 & 0 & 0 & 0 & 0 & 0 \\ 0 & \mathbf{I} & 0 & 0 & 0 & 0 & \dots & 0 & 0 & 0 & 0 & 0 & 0 \\ \mathbf{K} & \mathbf{C} & \mathbf{M} & 0 & 0 & 0 & \dots & 0 & 0 & 0 & 0 & 0 & 0 \\ \mathbf{L}_1 & \mathbf{L}_2 & \mathbf{L}_3 & \mathbf{K}_{\text{eff}} & 0 & 0 & \dots & 0 & 0 & 0 & 0 & 0 & 0 \\ a_1\mathbf{I} & \mathbf{I} & 0 & -a_1\mathbf{I} & \mathbf{I} & 0 & \dots & 0 & 0 & 0 & 0 & 0 & 0 \\ a_0\mathbf{I} & a_2\mathbf{I} & \mathbf{I} & -a_0\mathbf{I} & 0 & \mathbf{I} & \dots & 0 & 0 & 0 & 0 & 0 & 0 \\ \vdots & \vdots & \vdots & \vdots & \vdots & \vdots & \ddots & \vdots & \vdots & \vdots & \vdots & \vdots & \vdots \\ 0 & 0 & 0 & 0 & 0 & 0 & \dots & \mathbf{L}_1 & \mathbf{L}_2 & \mathbf{L}_3 & \mathbf{K}_{\text{eff}} & 0 & 0 \\ 0 & 0 & 0 & 0 & 0 & 0 & \dots & a_1\mathbf{I} & \mathbf{I} & 0 & -a_1\mathbf{I} & \mathbf{I} & 0 \\ 0 & 0 & 0 & 0 & 0 & 0 & \dots & a_0\mathbf{I} & a_2\mathbf{I} & \mathbf{I} & -a_0\mathbf{I} & 0 & \mathbf{I} \end{bmatrix}, \tag{B.1}$$

where:

$$\mathbf{K}_{\text{eff}} = a_0\mathbf{M} + a_1\mathbf{C} + \mathbf{K}, \quad \mathbf{L}_1 = -a_0\mathbf{M} - a_1\mathbf{C}, \quad \mathbf{L}_2 = -a_2\mathbf{M} - \mathbf{C}, \quad \mathbf{L}_3 = -\mathbf{M},$$
$$a_0 = \frac{4}{(\Delta t)^2},\ a_1 = \frac{2}{\Delta t},\ a_2 = \frac{4}{\Delta t}, \tag{B.2}$$

with Δt denoting time step. The vector $\hat{\mathbf{d}}$, which encompasses the space-time discretization of the unknown nodal quantities at all time steps, is defined as:

$$\hat{\mathbf{d}} = \begin{bmatrix} \hat{\mathbf{U}} \\ \dot{\hat{\mathbf{U}}} \\ \ddot{\hat{\mathbf{U}}} \end{bmatrix}, \tag{B.3}$$

where $\hat{\mathbf{U}}$, $\dot{\hat{\mathbf{U}}}$, $\ddot{\hat{\mathbf{U}}}$ are the space-time discretization of displacement-like quantities $\mathbf{U}(t)$, the velocity-like $\dot{\mathbf{U}}(t)$, and the acceleration-like $\ddot{\mathbf{U}}(t)$, respectively. Specifically:

$$\hat{\mathbf{U}} = \begin{bmatrix} \mathbf{U}_{i_0} \\ \mathbf{U}_{d_0} \\ \mathbf{V}_0 \\ \vdots \\ \mathbf{U}_{i_\tau} \\ \mathbf{U}_{d_\tau} \\ \mathbf{V}_\tau \end{bmatrix}, \quad \dot{\hat{\mathbf{U}}} = \begin{bmatrix} \dot{\mathbf{U}}_{i_0} \\ \dot{\mathbf{U}}_{d_0} \\ \dot{\mathbf{V}}_0 \\ \vdots \\ \dot{\mathbf{U}}_{i_\tau} \\ \dot{\mathbf{U}}_{d_\tau} \\ \dot{\mathbf{V}}_\tau \end{bmatrix}, \quad \ddot{\hat{\mathbf{U}}} = \begin{bmatrix} \ddot{\mathbf{U}}_{i_0} \\ \ddot{\mathbf{U}}_{d_0} \\ \ddot{\mathbf{V}}_0 \\ \vdots \\ \ddot{\mathbf{U}}_{i_\tau} \\ \ddot{\mathbf{U}}_{d_\tau} \\ \ddot{\mathbf{V}}_\tau \end{bmatrix}, \tag{B.4}$$

where subscripts $0 \dots \tau$ indicate time steps, with τ denoting the final time step; in the above, $\mathbf{U}(t)$ is defined as in (4):

$$\mathbf{U}(t) = \begin{bmatrix} \mathbf{U}_i^T(t) & \mathbf{U}_d^T(t) & \mathbf{V}^T(t) \end{bmatrix}^T = \begin{bmatrix} \mathbf{U}_i^T(t) & \mathbf{U}_d^T(t) & \mathbf{W}_e^T(t) & \boldsymbol{\Theta}^T(t) & \boldsymbol{\Phi}^T(t) & \mathbf{H}^T(t) \end{bmatrix}^T . \tag{B.5}$$

References

[1] Y. M. Hashash, D. Park, Viscous damping formulation and high frequency motion propagation in non-linear site response analysis, Soil Dynamics and Earthquake Engineering 22 (2002) 611–624.

[2] J. Garcia-Suarez, E. Seylabi, D. Asimaki, Linear one-dimensional site response analysis in the presence of stiffness-less free surface for certain power-law heterogeneities, Soil Dynamics and Earthquake Engineering 141 (2021) 106530. doi:https://doi.org/10.1016/j.soildyn.2020.106530.

[3] L. Mejia, E. Dawson, Earthquake deconvolution for FLAC, Fourth International FLAC Symposium on Numerical Modeling in Geomechanics, 2006.

[4] M. K. Poul, A. Zerva, Efficient time-domain deconvolution of seismic ground motions using the equivalent-linear method for soil-structure interaction analyses, Soil Dynamics and Earthquake Engineering 112 (2018) 138 – 151. URL: http://www.sciencedirect.com/science/article/pii/S0267726117305742. doi:https://doi.org/10.1016/j.soildyn.2018.04.032.

[5] M. K. Poul, A. Zerva, Nonlinear dynamic response of concrete gravity dams considering the deconvolution process, Soil Dynamics and Earthquake Engineering 109 (2018) 324 – 338. URL: http://www.sciencedirect.com/science/article/pii/S0267726117308825. doi:https://doi.org/10.1016/j.soildyn.2018.03.025.

[6] H. Bao, J. Bielak, O. Ghattas, L. F. Kallivokas, D. R. O'Hallaron, J. R. Shewchuk, J. Xu, Large-scale simulation of elastic wave propagation in heterogeneous media on parallel computers, Computer methods in applied mechanics and engineering 152 (1998) 85–102.

[7] V. Akçelik, G. Biros, O. Ghattas, Parallel multiscale Gauss-Newton-Krylov methods for inverse wave propagation, in: Supercomputing, ACM/IEEE 2002 Conference, IEEE, 2002, pp. 41–41.

[8] V. Akçelik, J. Bielak, G. Biros, I. Epanomeritakis, O. Ghattas, L. F. Kallivokas, E. J. Kim, A framework for online inversion-based 3D site characterization, in: Lecture Notes in Computer Science, Computational Science, volume 3038/2004, 2004, pp. 717–724.

[9] W. Zhang, D. Restrepo, J. G. Crempien, B. Erkmen, R. Taborda, A. Kurtulus, E. Taciroglu, A computational workflow for rupture-to-structural-response simulation and its application to istanbul, Earthquake Engineering & Structural Dynamics 50 (2021) 177–196. doi:https://doi.org/10.1002/eqe.3377.

[10] J. Bielak, K. Loukakis, Y. Hisada, C. Yoshimura, Domain reduction method for three-dimensional earthquake modeling in localized regions, Part I: Theory, Bulletin of the Seismological Society of America 93 (2003) 817–824.

[11] C. Yoshimura, J. Bielak, Y. Hisada, A. Fernández, Domain reduction method for three-dimensional earthquake modeling in localized regions, part II: Verification and applications, Bulletin of the Seismological Society of America 93 (2003) 825–841.

[12] B. Guidio, H. Goh, C. Jeong, Effective seismic force retrieval from surface measurement for SH-wave reconstruction, Soil Dynamics and Earthquake Engineering 165 (2023) 107682. URL: https://www.sciencedirect.com/science/article/pii/S0267726122005279. doi:https://doi.org/10.1016/j.soildyn.2022.107682.

[13] B. Poursartip, A. Fathi, L. F. Kallivokas, Seismic wave amplification by topographic features: A parametric study, Soil Dynamics and Earthquake Engineering 92 (2017) 503–527. URL: http://www.sciencedirect.com/science/article/pii/S0267726116304559. doi:10.1016/j.soildyn.2016.10.031.

[14] B. Poursartip, L. F. Kallivokas, Model dimensionality effects on the amplification of seismic waves, Soil Dynamics and Earthquake Engineering 113 (2018) 572–592. URL: https://www.sciencedirect.com/science/article/pii/S0267726117309570. doi:https://doi.org/10.1016/j.soildyn.2018.06.012.

[15] W. Zhang, E. E. Seylabi, E. Taciroglu, An ABAQUS toolbox for soil-structure interaction analysis, Computers and Geotechnics 114 (2019) 103143. URL: http://www.sciencedirect.com/science/article/pii/S0266352X19302071. doi:https://doi.org/10.1016/j.compgeo.2019.103143.

[16] S. François, H. Goh, L. F. Kallivokas, Non-convolutional second-order complex-frequency-shifted perfectly matched layers for transient elastic wave propagation, Computer Methods in Applied Mechanics and Engineering 377 (2021) 113704. URL: https://www.sciencedirect.com/science/article/pii/S0045782521000402. doi:https://doi.org/10.1016/j.cma.2021.113704.

[17] S. François, H. Goh, L. F. Kallivokas, Corrigendum to "non-convolutional second-order complex-frequency-shifted perfectly matched layers for transient elastic wave propagation", Computer Methods in Applied Mechanics and Engineering 400 (2022) 115578.

[18] T. Walsh, W. Aquino, M. Ross, Source Identification in Acoustics and Structural Mechanics using SIERRA/SD, Technical Report, Sandia National Laboratories, 2013. URL: https://prod-ng.sandia.gov/techlib-noauth/access-control.cgi/2013/132689.pdf.

[19] B. P. Guidio, C. Jeong, Full-waveform inversion of incoherent dynamic traction in a bounded 2D domain of scalar wave motions, Journal of Engineering Mechanics 147 (2021) 04021010. doi:10.1061/(ASCE)EM.1943-7889.0001909.

[20] R. Courant, D. Hilbert, Methods of Mathematical Physics, Vol. II., ISBN 0-471-50439-4, John Wiley & Sons, 1989.

[21] S. Ghahari, F. Abazarsa, E. Taciroglu, Probabilistic blind identification of site effects from ground surface signals, Bulletin of Earthquake Engineering 16 (2018) 1079–1104.

[22] S. Ghahari, F. Abazarsa, C. Jeong, A. Kurtulus, E. Taciroglu, Blind identification of site effects and bedrock motion from surface response signals, Soil Dynamics and Earthquake Engineering 107 (2018) 322 – 331. doi:https://doi.org/10.1016/j.soildyn.2018.01.045.

[23] G. Li, Y. Xue, R. Wang, H. Zhang, Z. Dong, D. Yu, Multiphase wavefield inversion methodology for seismic analysis of soil-structure interaction systems, Soil Dynamics and Earthquake Engineering 173 (2023) 108081. doi:https://doi.org/10.1016/j.soildyn.2023.108081.

[24] A. Fathi, B. Poursartip, L. F. Kallivokas, Time-domain hybrid formulations for wave simulations in three-dimensional PML-truncated heterogeneous media, International Journal for Numerical Methods in Engineering 101 (2015) 165–198.

[25] D. Assimaki, L. Kallivokas, J. Kang, W. Li, S. Kucukcoban, Time-domain forward and inverse modeling of lossy soils with frequency-independent Q for near-surface applications, Soil Dynamics and Earthquake Engineering 43 (2012) 139–159.

[26] B. Guidio, B. Jeremić, L. Guidio, C. Jeong, Passive seismic inversion of SH wave input motions in a truncated domain, Soil Dynamics and Earthquake Engineering 158 (2022) 107263. doi:https://doi.org/10.1016/j.soildyn.2022.107263.

[27] J. M. Roësset, D.-W. Chang, K. H. Stokoe, M. Aouad, Modulus and thickness of the pavement surface layer from SASW tests, Transportation Research Record (1990).

[28] B. A. Luke, K. H. Stokoe, Application of SASW Method Underwater, Journal of Geotechnical and Geoenvironmental Engineering 124 (1998) 523–531. doi:10.1061/(ASCE)1090-0241(1998)124:6(523).
[29] L. T. Brown, D. M. Boore, K. H. Stokoe, Comparison of shear-wave slowness profiles at 10 strong-motion sites from noninvasive SASW measurements and measurements made in boreholes, Bulletin of the Seismological Society of America 92 (2002) 3116–3133.
[30] B. R. Cox, D. P. Teague, Layering ratios: a systematic approach to the inversion of surface wave data in the absence of a priori information, Geophysical Journal International 207 (2016) 422–438.
[31] D. P. Teague, B. R. Cox, E. M. Rathje, Measured vs. predicted site response at the Garner Valley Downhole Array considering shear wave velocity uncertainty from borehole and surface wave methods, Soil Dynamics and Earthquake Engineering 113 (2018) 339–355.
[32] C. B. Park, R. D. Miller, J. Xia, Multichannel analysis of surface waves, Geophysics 64 (1999) 800–808.
[33] S. Rahimi, C. M. Wood, A. K. Himel, Application of microtremor horizontal to vertical spectra ratio (MHVSR) and multichannel analysis of surface wave (MASW) for shallow bedrock mapping for transportation projects, in: Geo-Congress 2020: Modeling, Geomaterials, and Site Characterization, American Society of Civil Engineers Reston, VA, 2020, pp. 622–632.
[34] A. Fathi, L. F. Kallivokas, B. Poursartip, Full-waveform inversion in three-dimensional PML-truncated elastic media, Computer Methods in Applied Mechanics and Engineering 296 (2015) 39–72.
[35] A. Fathi, B. Poursartip, K. H. Stokoe, L. F. Kallivokas, Three-dimensional P-and S-wave velocity profiling of geotechnical sites using full-waveform inversion driven by field data, Soil Dynamics and Earthquake Engineering 87 (2016) 63–81. URL: http://www.sciencedirect.com/science/article/pii/S0267726116300148.
[36] L. Kallivokas, A. Fathi, S. Kucukcoban, K. Stokoe, J. Bielak, O. Ghattas, Site characterization using full waveform inversion, Soil Dynamics and Earthquake Engineering 47 (2013) 62–82.
[37] J. Lysmer, R. L. Kuhlemeyer, Finite dynamic model for infinite media, Journal of Engineering Mechanics Division, ASCE 95 (1969) 859–877.